

Bachelor's Thesis

Steering excited state dynamics of biological chromophores by external electric fields.

prepared by

Fabian Knoch

from Marburg

at the Max Planck Institute for Biophysical Chemistry, Göttingen
Department for Theoretical and Computational Biophysics

Thesis period: 1st May 2011 until 1st September 2011

First Referee: Dr. Gerrit Groenhof

Second Referee: Prof. Dr. Helmut Grubmüller

Contents

1. Introduction	1
2. Theory	3
2.1. Methods of Quantum Chemistry	3
2.1.1. Born-Oppenheimer Approximation	3
2.1.2. Time Independent Hartree-Fock Theory	4
2.1.3. Configuration Interaction Method	7
2.2. Photoisomerization	9
3. The Biological System	11
3.1. Natural Origin and Structure of pCK ⁻	11
3.2. Charge Distribution and First Excited State	13
4. Static Calculations	17
4.1. Computational Details	17
4.2. Double Bond Twist	20
4.3. Single Bond Twist	24
4.4. Influence of the Field & Active Space	27
5. Dynamics	29
5.1. Simulation Setup and Computational Details	29
5.1.1. Simulation Setup	29
5.1.2. Computational Details	31
5.1.3. Ground State Ensemble	32
5.2. Control of the Single/Double Bond Twist	33
5.3. Radiationless Decay	35
5.4. Absorption Spectra	38

Contents

5.5. Spontaneous Emission	39
6. Conclusion & Outlook	41
A. Appendix	43

Nomenclature

Greek & Latin Letters

Variable	Meaning
α	Single Bond Torsion Angle
β	Double Bond Torsion Angle
S_0	Ground State Potential Energy Surface
S_1	First Excited State Potential Energy Surface

Abbreviation

Abbreviation	Meaning
TISE	Time-Independent Schrödinger Equation
PES	Potential Energy Surface
HF	Hartree-Fock
RHF	Restricted Hartree-Fock
CI	Configuration Interaction
CSF	Configuration state function
MO	Molecular Orbital
CASSCF	Complete Active Space Self-Consistent Field
pCA	Para-Couramic Acid
PYP	Photoactive Yellow Protein
pCK ⁻	Para-Couramic Ketone
SB	Single Bond
DB	Double Bond
SB _{min}	Single Bond Twisted Minimum Structure

Nomenclature

Abbreviation	Meaning
DB _{min}	Double Bond Twisted Minimum Structure
EOM-CCSD	Equation of Motion Coupled Cluster for Single and Double Excitations
QM/MM	Quantum Mechanics / Molecular Mechanics
FC	Franck-Condon
HOMO	Highest Occupied Molecular Orbital
LUMO	Lowest Unoccupied Molecular Orbital

1

Introduction

Photochemical processes play a key role in biological systems. In such processes, photons are absorbed by biological molecules and trigger chemical reactions. Photoisomerization, a type of photochemical process which produces an isomer of the original molecule, plays a crucial role in many biological systems. In photoisomerization, the energy landscape of the excited molecule changes when a photon is absorbed, causing the molecule to rearrange into an isomer. Several different applications of photoisomerization are observed in nature. In the retinal chromophore, which is part of the photoreceptors in most vertebrates, photoisomerization is responsible for the initiation of visual phototransduction [23]. In *Halobacterium salinarium* the same chromophore functions as a molecular engine which pumps protons through a cell membrane, [2]. In both of these cases, the initial reaction is triggered by ultra-fast double bond isomerization on time scales less than a picosecond. This type of reaction is not only ultra-fast but is also very efficient and therefore offers great potential for many applications. Ultra-fast photoisomerization is connected to a conical intersection where the potential energy surfaces of the ground and excited state intersect, leading to a fast and radiationless decay of the excited molecule back to the ground state. For a deeper insight into protein functions it is crucial to understand and even control the photoisomerization process. A possible control

1. Introduction

mechanism is already provided in the protein environment. Strong, local electric fields are established by hydrogen bonds or charged side chains. In the following thesis, a method for steering this photoisomerization processes via external electric fields is presented. Electric fields are relatively easy to apply on small scales, and the current feasible permanent field strengths are sufficient to affect the energy levels of molecules with more than a few electrons.

As a proof of concept, one of the simplest biological systems, an analogue of the photoactive yellow protein (PYP) chromophore, has been selected for numerical study of photoisomerization processes with high accuracy. Time-resolved simulations can be accomplished with reasonable effort, so that conical intersections can be observed. The investigated molecule is treated in vacuo, not only for computational efficiency but also to neglect further non-field-dependent influences. The reaction pathway is investigated to determine whether the pathway is sensitive to the presence of electric fields. Following a short theoretical introduction on quantum chemistry methods, the biological origin, structure and charge distribution of the selected chromophore will be discussed. Subsequently, the topologies of the ground and first excited state under the influence of electric fields are examined. Finally, time-resolved simulations are performed that qualitatively validate the topologies and allow prediction of reaction rates and absorption spectra which can be experimentally verified.

2

Theory

2.1. Methods of Quantum Chemistry

2.1.1. Born-Oppenheimer Approximation

The first step for modeling the quantum mechanical properties of molecules is to derive the time-independent Schrödinger equation (TISE) and its Hamiltonian \mathbf{H} , which is given as the sum over the kinetic \mathbf{T} and potential energy \mathbf{V} for each particle. The potential energy terms will only include the Coulomb interaction between all particles of the molecule if relativistic effects are neglected (which is reasonable as biomolecules are generally composed of first and second row elements). Thus, the TISE and its Hamiltonian can be written as

$$\mathbf{H}\psi(\mathbf{r}_e, \mathbf{R}_N) = E\psi(\mathbf{r}_e, \mathbf{R}_N) \quad (2.1)$$

$$\mathbf{H} = T_N + T_e + V_{NN} + V_{eN} + V_{ee} \quad (2.2)$$

where E is the total energy of the molecule and ψ an eigenfunction. The subscript N belongs to the nuclei and e to the electrons whereas the nucleus-nucleus dependency is represented by NN , the electron-nucleus one by eN and the electron-electron

2. Theory

dependency by ee . The wave function ψ depends on the nuclear \mathbf{R}_N and electronic positions \mathbf{r}_e . In general, there does not exist an analytical solution for the TISE (Eq. 2.1) and even numerical calculations are computationally intensive. J. Robert Oppenheimer and M. Born introduced an approximation in 1927 to simplify the TISE which allows the TISE to be separated into an electronic and a nuclear equation and solved separately.

The electronic TISE

$$\underbrace{(T_e + V_{eN} + V_{ee} + V_{NN})}_{=\mathbf{H}_e} \psi_e(\mathbf{r}_e; \mathbf{R}_N) = U(\mathbf{R}_N) \psi_e(\mathbf{r}_e; \mathbf{R}_N) \quad (2.3)$$

needs to be solved where $U(\mathbf{R}_N)$ represents the electronic eigenvalue. ψ_e is a function of \mathbf{r}_e and relies only parametrically on the nuclear positions \mathbf{R}_N . In other words, the nuclear positions are fixed. This assumption is physically because the mass of an electron is orders of magnitude smaller than the mass of the nuclei ($m_e \ll m_n$). Hence, the velocities of the electrons are much higher than that of the nuclei, and therefore the electronic movement can be considered to adjust instantly to the nuclear movement.

$U(\mathbf{R}_N)$ forms an potential energy surface (PES) for the nuclei (see Eq. 2.3), and thus the nuclear TISE is

$$\underbrace{(T_N + U)}_{=\mathbf{H}_N} \psi(\mathbf{R}_N) = E \psi(\mathbf{R}_N). \quad (2.4)$$

As a consequence of the Born-Oppenheimer approximation different electronic states create different but well-defined potential energy surfaces that cannot intersect. This consequence of the approximation does not always reflect reality and can lead to errors, see Section 2.2.

2.1.2. Time Independent Hartree-Fock Theory

Even after applying the Born-Oppenheimer Approximation the electronic TISE cannot be solved analytically, and therefore numerical approximation methods are required. The basis for many numerical approximation methods with different depth of theory is given by the Hartree-Fock method. As mentioned in Section 2.1.1, the electronic wave function and energy depend only parametrically on the nuclear

coordinates \mathbf{R}_N . Hence, the Hamiltonian of Eq. 2.3 follows as:

$$\mathbf{H}_e = \underbrace{-\frac{\hbar}{2m_e} \sum_{i=1}^n \nabla_i^2}_{\text{kinetic energy}} - \underbrace{\sum_{\alpha=1}^N \sum_{i=1}^n \frac{Z_\alpha e'^2}{r_{\alpha i}}}_{V_{eN}} + \underbrace{\sum_{i=1}^{n-1} \sum_{j=i+1}^n \frac{e'^2}{r_{ij}}}_{V_{ee}} + \underbrace{\sum_{\alpha=1}^{N-1} \sum_{\beta=\alpha+1}^N \frac{Z_\alpha Z_\beta e'^2}{r_{\alpha\beta}}}_{V_{NN}} \quad (2.5)$$

Coulomb interaction

where i and j are the electron indices and α and β the nuclear ones. Furthermore, $e' = \frac{1}{4\pi\epsilon_0}$ is the prefactor of the Coulomb potential. $r_{ij} = |\mathbf{r}_i - \mathbf{r}_j|$, for instance, is the distance between two particles. Thus, Eq. 2.5 represents a n-body problem, which makes it impossible to solve analytically. The task is to find the eigenfunctions $|\psi\rangle$ and the energy E corresponding to the Schrödinger equation (Eq. 2.3). In Hartree-Fock (HF) theory, the total wave function is expressed through a single Slater determinant which is an antisymmetrized product approach of single electron wave functions and therefore obeys the Pauli principle. Together with the mean field interaction of the electrons, the n-body problem splits up into n coupled 1-body problems. The total wave function follows as

$$\psi_{SL} = \frac{1}{\sqrt{N!}} \begin{vmatrix} \phi_1(\mathbf{x}_1) & \phi_2(\mathbf{x}_1) & \dots & \phi_N(\mathbf{x}_1) \\ \phi_1(\mathbf{x}_2) & \phi_2(\mathbf{x}_2) & \dots & \phi_N(\mathbf{x}_2) \\ \vdots & \vdots & \ddots & \vdots \\ \phi_1(\mathbf{x}_N) & \phi_2(\mathbf{x}_N) & \dots & \phi_N(\mathbf{x}_N) \end{vmatrix} \quad (2.6)$$

where (\mathbf{x}_N) represents the spin and spacial coordinates $\mathbf{x} = \{\mathbf{r}, \omega\}$ of the n-th electron and ϕ_N the n-th spin-orbital wave function which is the product of the spacial and spin wave function.

After applying \mathbf{H}_e to ψ_{SL} the eigenvalues E become:

$$E = \sum_{i=1}^n h_i + \frac{1}{2} \sum_{i,j}^n (C_{ij} - A_{ij}) \quad \text{with,} \quad (2.7)$$

$$C_{ij} = \int \phi_i^*(\mathbf{x}_i) \phi_j^*(\mathbf{x}_j) \frac{e'^2}{|\mathbf{r}_i - \mathbf{r}_j|} \phi_i(\mathbf{x}_i) \phi_j(\mathbf{x}_j) d\mathbf{x}_i d\mathbf{x}_j \quad (2.8)$$

$$A_{ij} = \int \phi_i^*(\mathbf{x}_i) \phi_j^*(\mathbf{x}_j) \frac{e'^2}{|\mathbf{r}_i - \mathbf{r}_j|} \phi_j(\mathbf{x}_i) \phi_i(\mathbf{x}_j) d\mathbf{x}_i d\mathbf{x}_j \quad (2.9)$$

here h_i represents the i -th one electron energy, C_{ij} the Coulomb integral and A_{ij} the exchange integral. For a detailed derivation see [17]. The classical analogue of C_{ij}

2. Theory

is the repulsion energy between one electron occupying spin-orbital ϕ_i and another electron occupying spin-orbital ϕ_j . The exchange integral on the other hand has no classical analogue. To get as close as possible to the real electronic ground state energy, the derived energy has to be minimized. For this purpose, the variational principle is used with the orthonormalization constraint ($\langle\phi_i|\phi_j\rangle = \delta_{ij}$) of the wave function.

$$\delta L = \delta E - \sum_{i,j}^n \lambda_{ij} (\langle\delta\phi_i|\phi_j\rangle - \langle\phi_i|\delta\phi_j\rangle) = 0 \quad (2.10)$$

At this point, it is reasonable to define the Fock-operator \mathbf{F} which takes δE to the following form:

$$\mathbf{F}_i = \mathbf{h}_i + \sum_j^n (\mathbf{C}_j - \mathbf{A}_j) \quad (2.11)$$

$$\Rightarrow \delta E = \sum_i^n (\langle\delta\phi_i|\mathbf{F}_i|\phi_i\rangle + \langle\phi_i|\mathbf{F}_i|\delta\phi_i\rangle) \quad (2.12)$$

Inserting Eq. 2.12 into Eq. 2.10, the Hartree-Fock equation can be written as:

$$\mathbf{F}_i\phi_i = \sum_j^n \lambda_{ij}\phi_j \quad (2.13)$$

Subsequently, the last equation can be diagonalized, leading to an eigenvalue equation whose eigenvalues represent the canonical molecular orbital energies ε_i .

$$\mathbf{F}_i\phi'_i = \varepsilon_i\phi'_i \quad (2.14)$$

Hence, the ground state energy is given as follows:

$$E = \sum_i^n \varepsilon_i - \frac{1}{2} \sum_{i,j}^n (C_{ij} - A_{ij}) \quad (2.15)$$

The idea is to improve the ϕ'_i iteratively, by improving the electron densities in \mathbf{C} and \mathbf{A} until a convergence criterion is reached. Nevertheless, the HF energy is still an upper bound for the real ground state energy. Summing up HF theory, there are two important aspects to keep in mind:

- The wave function is expressed through a single Slater determinant which fulfills the Pauli principle.
- The electrons only notice the presence of each other via a mean field which is created by their charge density.

The latter is a drawback in HF theory because electron-electron correlation effects are neglected.

The question of the orbital initial conditions remains. Fortunately, every eigenfunction of a Hermitian operator can be expanded after a complete orthonormal basis where a_i are the molecular orbital (MO) coefficients and $|\chi_i\rangle$ are the atomic orbitals.

$$|\phi\rangle = \sum_{i=0}^n a_i |\chi_i\rangle \quad (2.16)$$

For numerical calculations, only a small number of elements of this expansion can be taken into account which are summarized in a basis set. Thus, the selection of the basis set has a serious influence of the accuracy of the HF energies as well as the molecular orbitals.

2.1.3. Configuration Interaction Method

As previously pointed out, HF theory fails when electron-electron correlation cannot be neglected. Unfortunately, an accurate prediction of binding energies and energy barriers, which is very important for this work, requires a more advanced level of quantum theory.

Over the past 50 years many different approximations for improving HF theory have been developed. One often used advanced approximation method is the Configuration Interaction (CI) method.

Due to mathematical complexity, only an outline of the CI is presented. For a more detailed derivation see [17].

The starting point of a CI calculation is MOs that have been either arbitrary chosen or calculated with a lower level of theory, which are composed of occupied and virtual (unoccupied) orbitals. In practice, Hartree-Fock MOs (ϕ'_i) are often used as the starting point of a CI calculation. The next step is to form configuration state functions (CSF) Φ_i by either a single Slater determinant or a linear combination of Slater determinants which include the ϕ'_i . The trial wave function ψ can be expressed through a linear combination of the configuration state function (CSF).

$$\psi = b_0\Phi_0 + \sum_S b_S\Phi_S + \sum_D b_D\Phi_D + \sum_T b_T\Phi_T + \dots = \sum_i b_i\Phi_i \quad (2.17)$$

Here 0 indicates no, S single, D double, and T triple excited Slater determinants relative to the starting configuration. The excited Slater determinants are created

2. Theory

by removing electrons of occupied orbitals, and placing them into virtual ones. The CI coefficients b_i are determined by the variational principle, similar to Section 2.1.2. Thus, not only the electronic correlation between already occupied orbitals but also between virtual ones are taken into account.

If the molecule has more than a few electrons, it will be impractical to consider all orbitals to evaluate ψ because the MO and CI coefficients have to be optimized independently. The computational effort required is infeasible, even for supercomputers. The number of CSFs ($\#_{\text{CSF}}$), which has to be optimized in the CI method, is given by

$$\#_{\text{CSF}} = \frac{c!(c+1)!}{(\frac{1}{2}n)!(\frac{1}{2}n+1)!(c-\frac{1}{2})!(c-\frac{1}{2}n+1)!} \quad (2.18)$$

where only singlet states are allowed ($S = 0$). c is the number of one electron basis functions and n the number of electrons. Table 2.1 shows the number of CSFs for the CH_3OH ($n = 18$) which demonstrates that even for comparatively

Table 2.1.: Number (#) of SCFs for CH_3OH for different basis sets [20]

basis set	c	# CSFs
STO-3G	14	$1 \cdot 10^6$
6-31G**	50	$7.6 \cdot 10^{17}$

small molecules an extensive basis set induces a large computational effort. In fact, with a small basis set the full CI is achievable at least for a few electrons but this does not guarantee an accurate solution. For high accuracy calculations a larger basis set is required, and therefore only a small number of orbitals can be included. The

included orbitals are consequently chosen such that they span the active space.

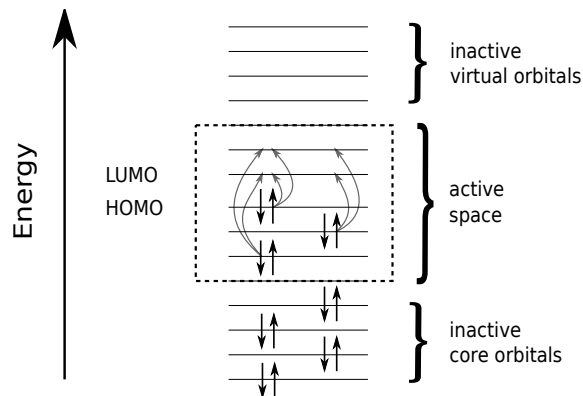


Figure 2.1.: Schematic overview of active and inactive space of the CASSCF method

In the complete active space self consistent field method (CASSCF) the full CI is performed within the active space. The challenge is to find the right active space

where the criterion of selection is mostly given by the electronic correlation between the MOs. Figure 2.1 illustrates the active and inactive space for the CASSCF method.

2.2. Photoisomerization

Photoisomerization plays a crucial role in many reactions in biochemistry and is the focus of this thesis. This chapter provides a qualitative description of two different kinds of photoisomerization processes.

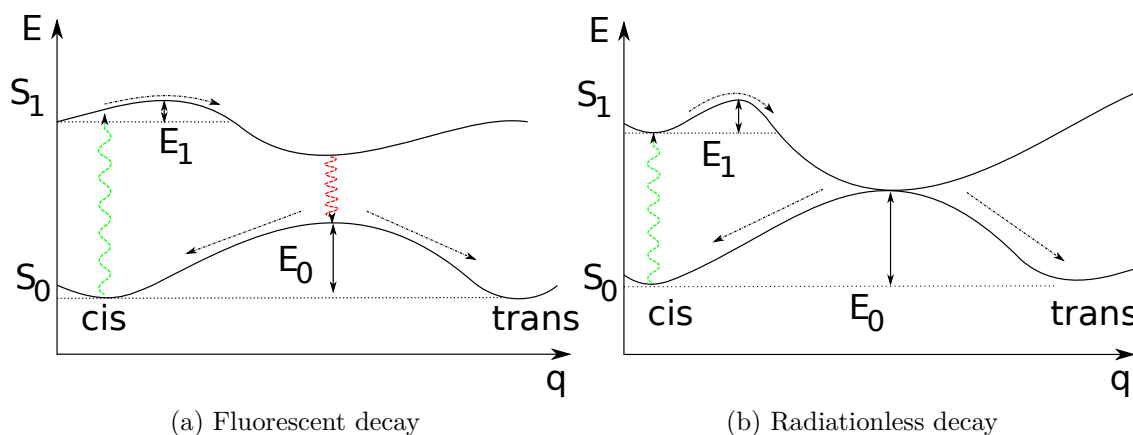


Figure 2.2.: Schematic overview of photoisomerization. The reaction coordinate q is plotted against the energy of states S_0 and S_1 . (a) shows an adiabatic transition from S_1 to S_0 via emission of a photon. (b) shows a non-adiabatic transition from S_1 to S_0 .

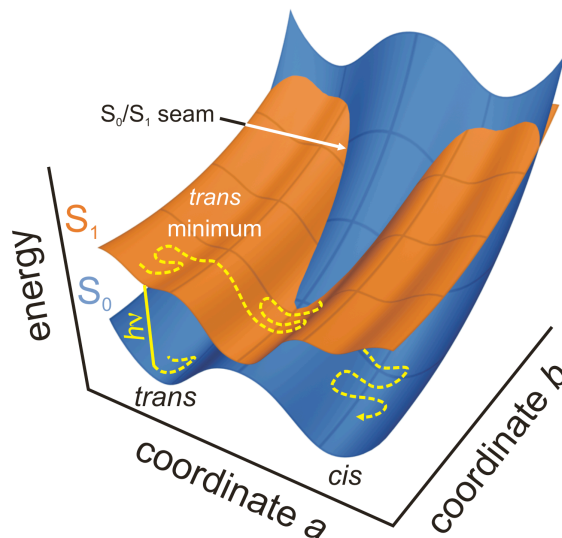
The system is situated in its ground state S_0 at a local minimum of a potential energy surface. To visualize this surface, at least one reaction coordinate q is needed, which is plotted against the energy of the system. The reaction coordinate could be, for instance, a bond length, a dihedral angle or any other attribute that characterizes a reaction. In the ground state the system is forced to remain in the minimum because of a barrier E_0 that cannot be crossed. When the system is excited by a photon, it evolves from the ground state to the first excited state S_1 . Due to the instant excitation of the system, the value of the reaction coordinate is fixed. In other words, the excitation must be represented vertically in Figure 2.2. However, in the S_1 state a barrier E_1 can also be located at the Franck-Condon region. In contrast to E_0 , the barrier E_1 is low and consequently can be passed. The system evolves to a deeper local minimum that causes a change in q , for example, a single

2. Theory

bond could convert to double bond, or the variation of an angle can lead to a twisted structure. Two different cases are considered in this work:

- After spending a time τ in the minimum of S_1 the system falls back to the ground state via emitting a photon. This transition is referred to as a fluorescent decay with τ being the fluorescent lifetime. Once returned to S_0 two possible paths can be taken. Either the system goes back to the starting minimum (cis) or it evolves to another minimum (trans) that causes a permanent change in q . The cycle is schematically shown in Figure 2.2a.
- In the second case, the energy surfaces S_0 and S_1 intersect or almost intersect when S_0 has its maximum and S_1 has its minimum. The system can evolve from S_1 to S_0 as a result of its vibrational modes. To be precise, the energy difference between the surfaces has to be on the order of or smaller than the separation between the vibrational energy levels, see [12]. At this point, the Born-Oppenheimer approximation (see Section 2.1.1) collapses because the different potential energy surfaces are no longer well-defined. The point where both surfaces intersect is called conical intersection and needs a different mathematical description. The conical intersection causes a radiationless decay (no photons are emitted) to the ground state. As mentioned before the system can evolve in two different ways. The radiationless cycle is illustrated in Figure 2.2b.

Figure 2.2 is a simplified model for photoisomerization. In reality the PES does not depend on just one reaction coordinate but on *degree of freedom minus six* coordinates. Therefore, the intersection is given by a multi-dimensional seam (see Figure 2.3 for three-dimensional PESs).



3

The Biological System

3.1. Natural Origin and Structure of pCK⁻

One of the most frequently described systems for photochemistry, especially for cis-trans photoisomerization, is given by the photoactive yellow protein (PYP) and its chromophore para-coumaric acid (pCA). The PYP was originally found

in the salt tolerant bacterium *Halorhodospira halophila* and has the role of a photoreceptor which is involved in the photomotility. To avoid damages, caused by ultra-violet radiation, the bacterium detects blue light and moves to the opposite direction of the gradient. Precisely, the chromophore absorbs blue light which triggers a fully reversible photo cycle with several intermediates on time scales between a few hundred femtoseconds and seconds [15, 24].

The PYP chromophore (Figure 3.1) is linked to the protein environment via a

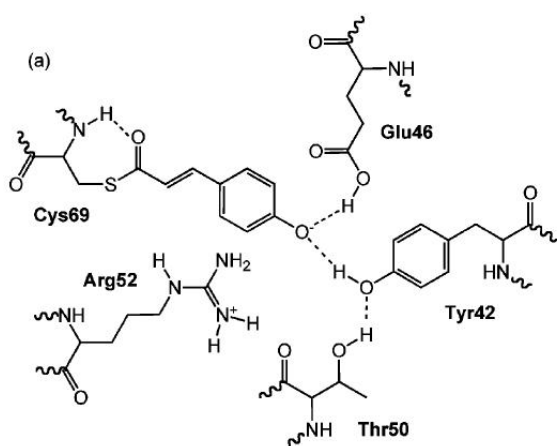


Figure 3.1.: Chromophore pCA in its natural environment as part of the photo active yellow protein (PYP) [7]

3. The Biological System

covalent thioester bond with a cysteine residue (Cys69). Furthermore, it experiences steric constraints imposed by the geometry of the active site as well as hydrogen bonds with several amino acids. In detail, it is Glu46 and Tyr42 on the phenolate side and Cys69 on the carbonyl side. Moreover, the chromophore is influenced by the electrostatic interaction of Arg52. In PYP, the chromophore is present in its anionic form which is suggested to play a crucial role in cis-trans photoisomerization and thus the biological function of the protein.

The chromophore which is investigated in the thesis is an analogue of the pCA. The acid group is substituted by a methyl group to maintain the anionic character where the net charge is -1. Figure 3.2 represents the structure of the p-couramic ketone (pCK^-) chromophore. Moreover, in the following work, only the ultra-fast cis-trans photoisomerization process which has already been observed in pCK^- [3] will be taken into account. In this work, three energy minima are important, two in the first excited state and one in the ground state, where each minimum corresponds to a different geometrical conformation.

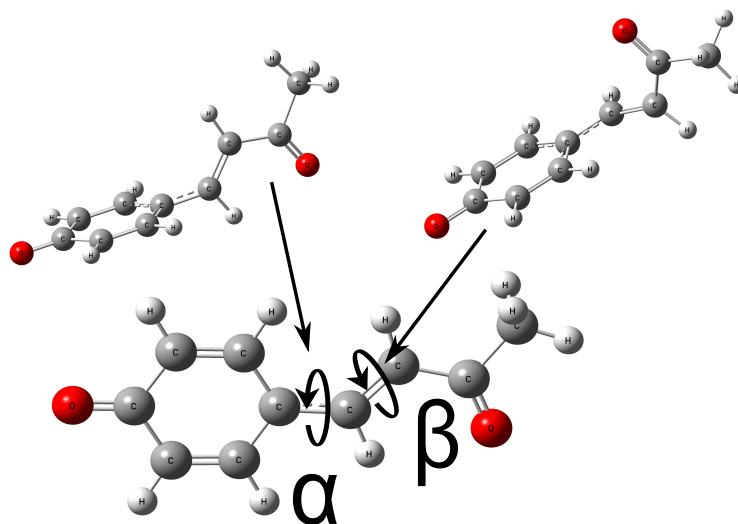


Figure 3.2.: pCK^- and its minimum structures. (Bottom) planar minimum structure. All carbon atoms are aligned in the same plane; (Top left) single bond minimum structure SB_{min} . The torsion angle $\alpha = 90^\circ$ relative to the planar minimum; (Top right) double bond minimum structure DB_{min} . The torsion angle $\beta = 90^\circ$ relative to the planar minimum.

In Figure 3.2 (bottom) both the phenolate and alkene moiety of the chromophore are located in the same plane and therefore this structure will be labeled as planar minimum. The second minimum (SB_{\min}) can be reached by a single bond (SB) twist of 90° and the third minimum (DB_{\min}) by a double bond (DB) twist of 90° . Figure 3.2 illustrates the possible structures. In contrast to the planar minimum, the SB_{\min} and DB_{\min} are only accessible via the first excited state S_1 (see Section 2.2) where the transition from the planar minimum to the respective excited state minimum is achieved on time scales less than one picosecond which is supported by several ab initio calculations ([3, 9]) as well as experimental data [6]. These time scales are not only increasing the reaction efficiency but are necessary to observe the isomerization process in simulations.

3.2. Charge Distribution and First Excited State

The pCK⁻ chromophore contains 86 electrons which are occupying 43 orbitals in the ground state. However, the important fact is that the first excited state is energetically well separated from its two neighbors.

Table 3.1.: Energy difference for excited states of pCK⁻, calculated using EOM-CCSD and Pople’s 6-31G* basis set.

	ΔE	wavelength	oscillator strength
$\Delta S_0 S_1$	2.7505 eV	450.76 nm	0.2565
$\Delta S_0 S_2$	4.3450 eV	285.35 nm	0.0977
$\Delta S_0 S_3$	4.5273 eV	273.86 nm	0.0216

Table 3.1 lists the energy differences from the ground to the first, second and third excited state as well as its corresponding excitation wavelength and oscillator strength¹. The separation of S_1 is very favorable as it ensures that only the first excited state gets occupied when the stimulating photons are within a certain energy interval. Otherwise, the photochemistry which will be investigated in the following chapters would be much more complicated. Another important fact for the following calculations is the symmetry of the ground and first excited state. According to Groenhof et al. [3, 9] as well as an EOM-CCSD calculation, both states belong to π orbitals, making the S_0/S_1 transition a π/π^* transition.

¹The oscillator strength refers to the transition from the ground state to the respective excited state.

3. The Biological System

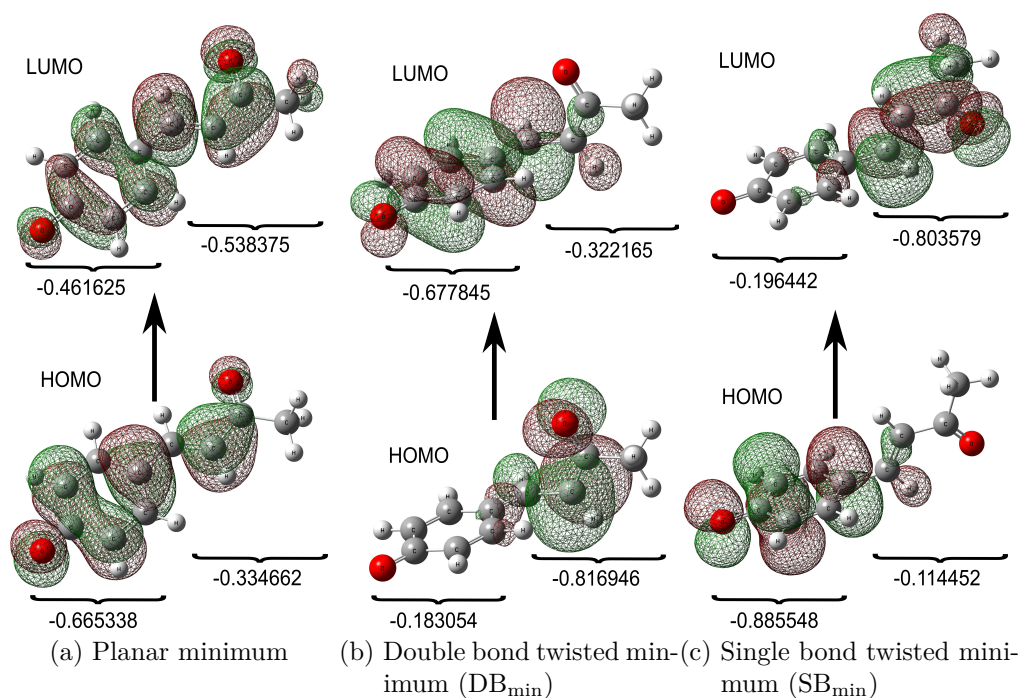


Figure 3.3.: HOMO and LUMO for single excitation as well as the mulliken charge distribution for both states and each minimum structure respectively. Note the charge transfer between the HOMO and LUMO.

Figure 3.3 presents the highest occupied molecular orbitals (HOMO) and the lowest unoccupied molecular orbitals (LUMO) for all minimum structures after performing a CASSCF(12e,11o) calculation. The computational details are listed in the following Section 4.1. For visualizing the charge distribution of all minimum structures, I assume that most of ground/first excited state, especially its transition, is essentially modulated by the HOMO/LUMO. In Figure 3.3a the electron density in the HOMO is slightly shifted to the phenolate ring compared to the LUMO where it is more favored over the alkene moiety. The density shift involves a charge transfer when the chromophore gets excited. Hence, the dipole moments μ_0 and μ_1 are pointing in different directions, even though the difference between both dipole moments is small. On the contrary, if pCK^- evolves to one of the other minimum structures, the shift becomes much more obvious which is demonstrated in Figure 3.3b and Figure 3.3c. For SB_{\min} (Fig. 3.3c) the electron density of the HOMO is exclusively placed on the phenolate ring, compared to the LUMO where it is completely transferred to the carbonyl tail. As a matter of fact, the charge separation is increased through the SB twist and therefore the dipole moment of the respective state is strengthened.

3.2. Charge Distribution and First Excited State

On the other hand, the DB twist (Fig. 3.3b) has the opposing effect. Here the LUMO occupies only the ring structure, whereas the HOMO is only located on the alkene moiety. However, the significant effect is given by the change of directions of the dipole moments and its absolute values, whether the chromophore is situated in SB_{min} or DB_{min}. For more quantitative evidence of the charge transfer please refer to the Mulliken charge distribution at the bottom of each structure in Figure 3.3. The charge transfer will play a key role for understanding the result in the subsequent chapters.

4

Static Calculations

The aim of this chapter is the investigation of the topology of the S_0 and S_1 state of pCK^- in vacuo with respect to external electric fields. The first section deals with the computational details, followed by the discussion of the topologies, for which both possible reaction coordinates (α and β), see Figure 3.3 on page 14, with their corresponding energies are evaluated. Subsequently, the field influence of the two excited state minimum structures is presented, followed by a short examination on the active space dependency of the topologies.

4.1. Computational Details

The calculations reported in this chapter have been achieved with the ab initio software package MOLPRO [26]. The first approach of evaluating the single point energies was obtained via the restricted Hartree-Fock (RHF) method. Afterwards, a geometry optimization has been performed. Subsequently, the canonical Hartree-Fock MOs were used as starting guesses for CASSCF calculations. Triplet states have not been considered, so the spin quantum number always stayed $S = 0$. The active space was chosen with respect to the expected π/π^* transition (see Section

4. Static Calculations

3.2 on page 13) and required 6 occupied (12 electrons) and 5 unoccupied MOs to include all π orbitals.

To be precise, Table 4.1 shows the necessary swapping of the orbitals to fulfill the required active space, including only π orbitals which inhibits n/π^* transitions. Furthermore, the CASSCF calculations were performed using the state averaging method of S_0 and S_1 where both weights were taken equally as 0.5. Throughout all calculations Pople's basis set 6-31G* was applied. The electric field was added as finite dipole field to the one electron Hamiltonian (see [14]).

Table 4.1.: Active space selection for CASSCF (12e,11o)

replaced MO numbers
41 \leftrightarrow 35
39 \leftrightarrow 34
47 \leftrightarrow 50
48 \leftrightarrow 54

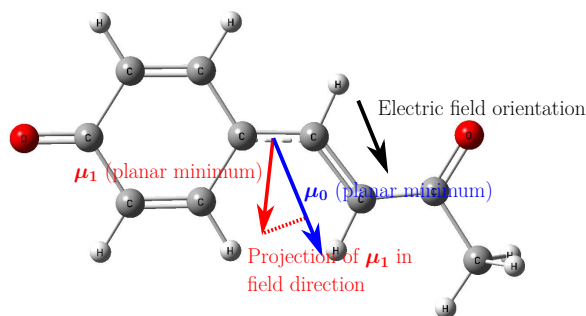


Figure 4.1.: Schematic overview of the electric field orientation

Moreover, the field direction equals the direction of the ground state dipole moment μ_0 which was calculated after the CASSCF(12e,11o) performance of the planar minimum structure. Thus, positive field values point parallel to μ_0 , whereas negative ones point anti-parallel¹. Figure 4.1 shows the orientation of the electric field, the ground and first excited state dipole moment. I believe the orientation of the electric field is reasonable because even in proteins the isomerization process is much faster than the adjustment of the excited molecule to the induced electric field lines, and therefore only at the Franck-Condon region the electric field points in the same direction as μ_0 . While simulating the single and double bond twisting processes, an adjustment to the field within 1 ps could not be observed. To obtain the PES the torsion angle, α or β , was successively increased from the PM to the SB_{min} or DB_{min} and beyond by $\Delta = 5^\circ$ with respect to a constant field strength. The twisting was achieved by holding the phenolate ring fix and rotating the carbonyl tail.

¹In the remaining thesis \mathbf{E} represents the electric field pointing in the same direction as the ground state dipole moment of the planar minimum.

Moreover, geometry optimizations have been performed for selected angles and field strengths. Table 4.2 lists the default convergence criteria of MOLPRO.

Table 4.2.: Convergence thresholds used by MOLPRO

	threshold [a.u.]		threshold [a.u.]
gradient	$1 \cdot 10^{-2}$	gradient	$3 \cdot 10^{-4}$
energy	$1.7 \cdot 10^{-6}$	energy	$1 \cdot 10^{-6}$
step length	$1 \cdot 10^{-3}$	step length	$3 \cdot 10^{-4}$

(a) CASSCF (b) Geometry optimization

4.2. Double Bond Twist

The DB twist corresponds to the change of the torsion angle β , see Figure 3.2 on page 12. The starting position of the rigid scan is the planar minimum, which is located at $\beta = 180^\circ$. As the second coordinate the electric field strength was taken into account. Therefore, the field strength was varied from $-50 \frac{\text{MV}}{\text{cm}} \leq \mathbf{E} \leq 50 \frac{\text{MV}}{\text{cm}}$, with $\Delta \mathbf{E} = 5.5 \frac{\text{MV}}{\text{cm}}$.

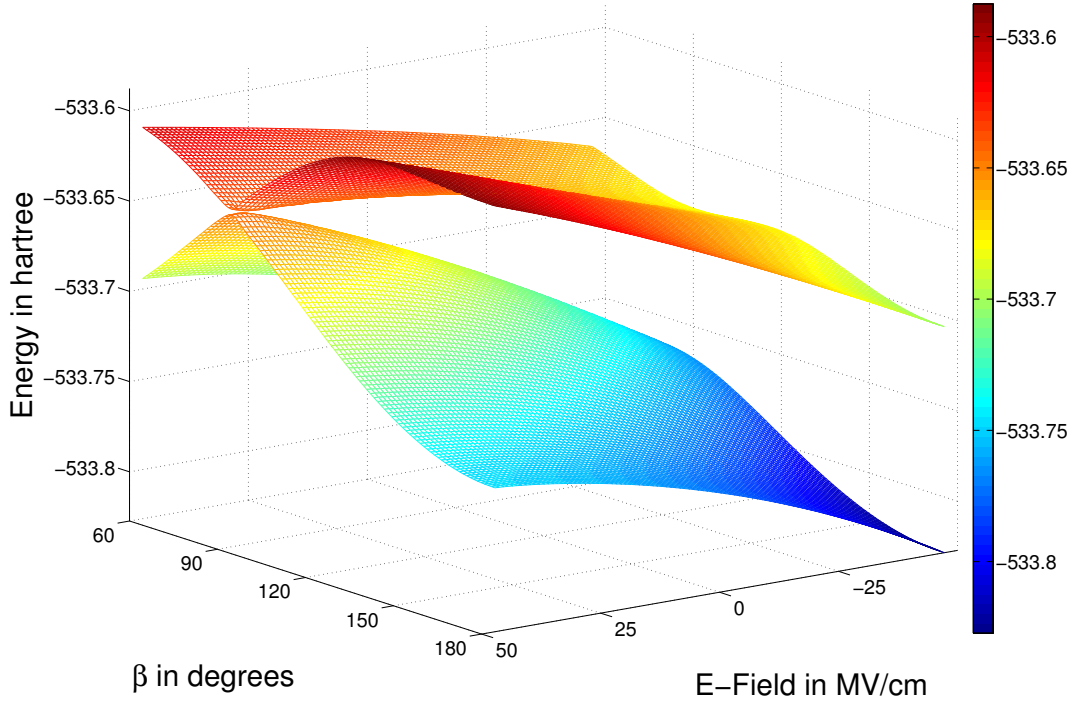


Figure 4.2.: The total energy of S_0 and S_1 is plotted against the electric field strength \mathbf{E} and the DB torsion angle β .

At $\beta = 90^\circ$ and $\mathbf{E} = 50 \frac{\text{MV}}{\text{cm}}$ Figure 4.2 shows a global maximum for S_0 and a minimum for S_1 . The corresponding structure can be identified as the double bond twisted minimum DB_{min} (see Fig. 3.2 on page 12). This PES indicates a photoisomerization including a conical intersection which leads to a radiationless decay. As a matter of fact, the general tendency can be observed that a stronger positive electric field lifts the energy of S_0 . At the Franck-Condon (FC) region ($\beta \approx 180^\circ$) this is reasonable as the field direction equals the direction of the dipole moment $\boldsymbol{\mu}_0$. On the other hand, the energy is lowered when the electric field points anti-parallel to the dipole moment. Both dipole moments $\boldsymbol{\mu}_0$ and

μ_1 show almost the same orientation at the FC region, see the charge distribution in Figure 3.3a on page 14, and therefore both surfaces elevate with increasing field strength. If β is twisting, the present dipole moment will change as well, thus, it does not point in the same direction as the external field anymore.

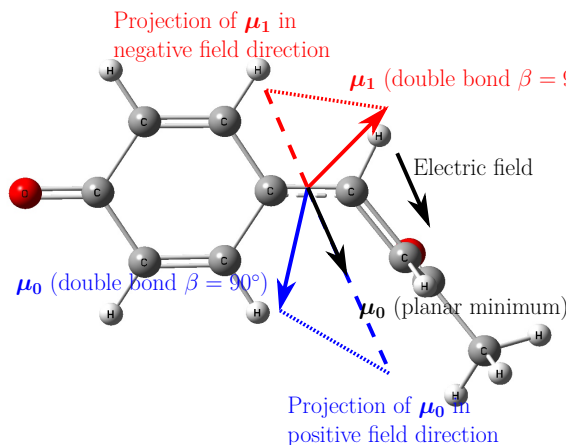


Figure 4.3.: Schematic overview of the orientations of the dipole moments

Nevertheless, the energy gradient in field direction of S_0 (see Figure 4.2) is increased while increasing the field strength, leading to global maximum for $\beta = 90^\circ$. The reason lies on the charge separation of DB_{min} , see Section 3.2. The absolute value of the dipole moment is increased, so that even the projection of μ_0 on the electric field vector, is larger than μ_0 of the planar minimum. To get a qualitative idea of the different dipole moments, see Figure 4.3. Unfortunately, quantitative data of the dipole moments cannot be presented as the chromophore has a non-zero net charge, and therefore the values of the dipole moments depend on the chosen origin.

For $\beta < 90^\circ$ the energy gradient in field direction decreases again as the charge separation is reversible. In contrast, the energy of S_1 becomes more negative for $\beta = 90^\circ$ and positive field strengths. Here the charge separation again increases the absolute value of μ_1 but it is even more important that the charge separation also partly inverts its direction in comparison to the field orientation. Hence, a component of μ_1 points anti-parallel to \mathbf{E} , leading to a local minimum for $\mathbf{E} = 50 \frac{\text{MV}}{\text{cm}}$ and $\beta = 90^\circ$.

Figure 4.4 on the next page shows the energy difference $|S_1 - S_0|$ as function of β and \mathbf{E} . Particularly, for $\mathbf{E} = 50 \frac{\text{MV}}{\text{cm}}$ and $\beta = 90^\circ$ an intersection point can be identified.

4. Static Calculations

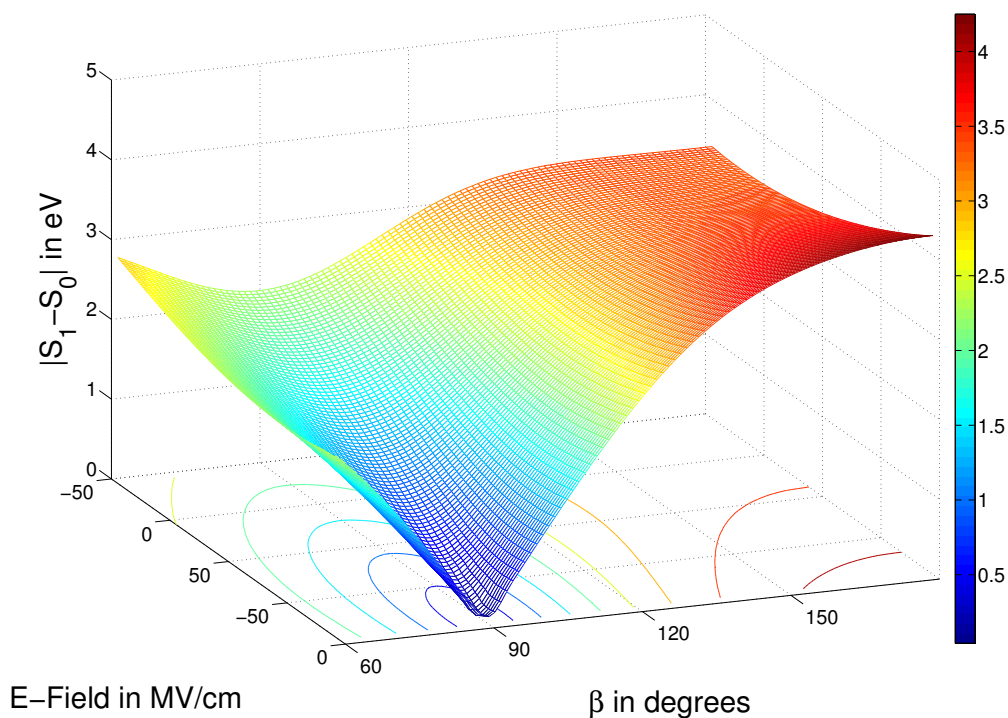


Figure 4.4.: The energy difference between S_1 and S_0 is plotted against \mathbf{E} and β .

The PESs were created without geometry optimization, otherwise the computational effort would be too high. Nevertheless, two energy two-dimensional section planes were calculated considering geometry optimizations, namely the planes for $\mathbf{E} \in \{0 \frac{\text{MV}}{\text{cm}}; 50 \frac{\text{MV}}{\text{cm}}\}$. It was not possible to perform geometry optimizations while applying electric fields neither with the MOLPRO nor the GAUSSIAN [8] software package. To obtain the optimized energies, geometry optimizations were performed without applied field and second energy calculations with applied field were started afterwards. I thus assume that the applied field strengths are not high enough to change the geometry of the molecule. The results are presented in Figure 4.5. The data reveal that the intersection of both states is also observable when applying the field and secondly, the reaction barrier disappears. Without field, the barrier is about $18 \frac{\text{kJ}}{\text{mol}}$ high, but with applied field only a saddle point instead of a maximum is recognizable.

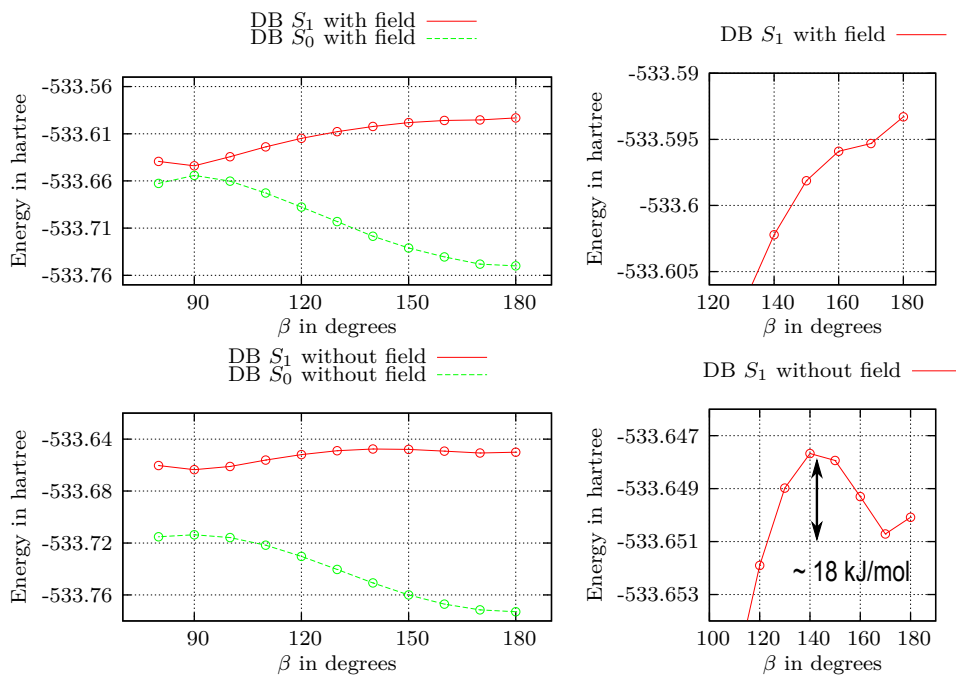


Figure 4.5.: Section planes of the DB topology. (Top left) with applied electric field $\mathbf{E} = 50 \frac{\text{MV}}{\text{cm}}$, (bottom left) without electric field. (Top right) zoom of the reaction barrier with applied field and (bottom right) without.

The key results of the DB topology examination are: At first, positive field strengths favor the DB twist and lead to conical intersections and secondly, the energy barrier that needs to be crossed to evolve into DB_{min} disappears while applying positive fields. Note, that the field orientations are relative to the ground state dipole moment of the planar minimum, see Section 4.1.

4.3. Single Bond Twist

The SB twist corresponds to the rotation of α (see section 3.1). Similar to Section 4.2, the PESs were obtained without geometry optimization, yet the two interesting section planes were treated separately with more accuracy. The evaluated interval for \mathbf{E} and the step size $\Delta\mathbf{E}$ are the same as in Section 4.2, the SB torsion angle α was varied from 180° to 60° with $\Delta\alpha = 5^\circ$. Figure 4.6 illustrates a global maximum of S_0 and a global minimum of S_1 for $\mathbf{E} = -50 \frac{\text{MV}}{\text{cm}}$ and $\alpha = 90^\circ$.

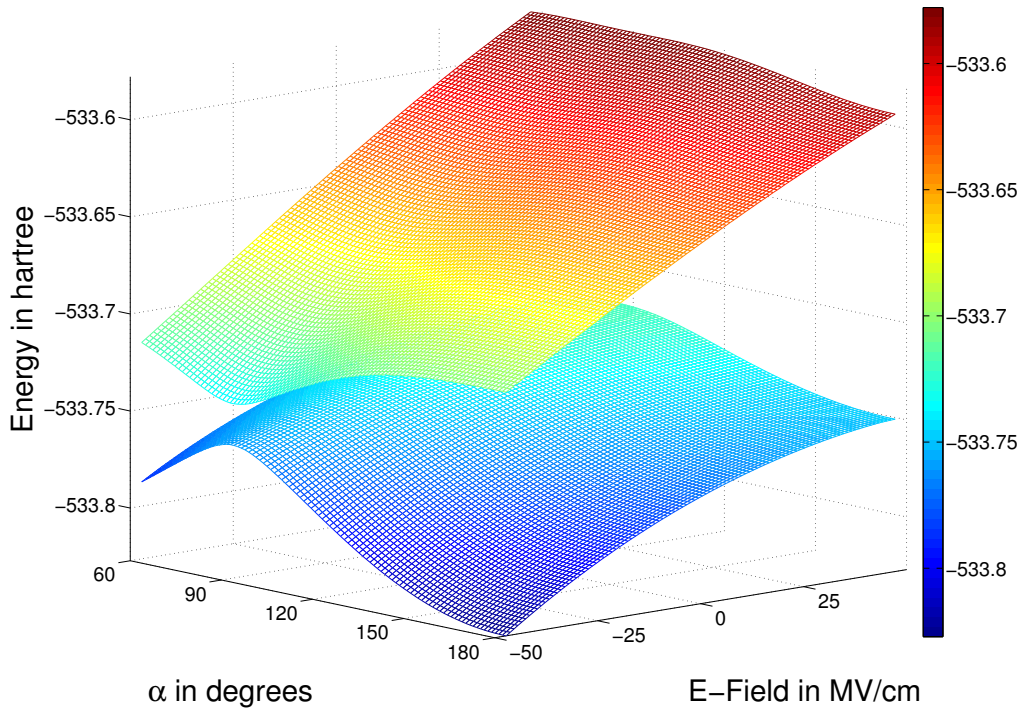


Figure 4.6.: The total energy of S_0 and S_1 is plotted against the electric field strength \mathbf{E} and the single bond torsion angle α .

In contrast to the DB twist, this point is achieved by a strong electric field opposite to the dipole moment of the planar minimum. The corresponding structure can be identified as the single point minimum structure SB_{min} (see Fig 3.2 on page 12). The reason for the local maximum in S_0 and minimum in S_1 - similar to the double bond topologies - is given by the strong charge separation of SB_{min} , which shows exactly the opposite behavior of the DB_{min} (see Section 3.2 and Figure 4.7). Here the gradient in field direction of S_1 is steeper than of S_0 , because for $\alpha = 90^\circ$, $\boldsymbol{\mu}_0$ is almost pointing perpendicular to the field direction. Instead of a conical

intersection, Fig. 4.6 still shows an energy gap, even though the electric field strength is comparatively high. Due to the gap, surface hopping between both states is rather unlikely, forcing the system to stay at S_1 . If the barrier near the minimum of S_1 is high and broad enough, the only possibility of falling back to S_0 will be via emission of a photon. A similar behavior of the surfaces is also observable at the

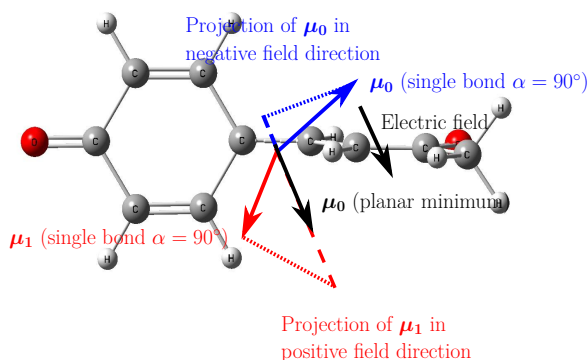


Figure 4.7.: Schematic overview of the orientations of the dipole moments

FC region ($\alpha \approx 180^\circ$) where both surfaces are lifted with increasing field strength as the respective dipole moments point in the same direction. However, an apparent difference between the surfaces in Fig. 4.2 is the smoothness of the curves. S_1 is rather even, whereas S_0 exhibits a larger curvature. The opposite behavior is demonstrated in Figure 4.6, where S_0 is flat compared to S_1 , leading to the assumption that the molecule evolves much quicker from the planar minimum to SB_{\min} than to DB_{\min} with respect to different field orientations. Further support comes from the observation of different heights of the energy barriers at the S_1 level. Figure 4.2 exhibits a much higher barrier than Figure 4.6 where no barrier is recognizable, leading to the conclusion that the SB twisted structure is favored, at least without applied field.

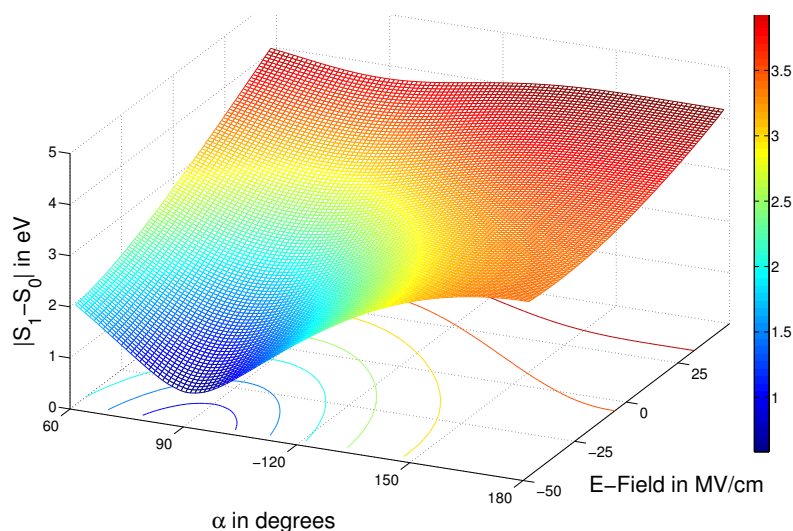


Figure 4.8.: The energy difference between S_1 and S_0 is plotted against \mathbf{E} and α

Figure 4.8 shows the energy difference between both states where an energy gap is observed for even a negative field strength of $-50 \frac{\text{MV}}{\text{cm}}$. After performing geometry

4. Static Calculations

optimizations of the two section planes where $\mathbf{E} \in \{-50 \frac{\text{MV}}{\text{cm}}, 0.0 \frac{\text{MV}}{\text{cm}}\}$, the observed energy barrier without electric field was negligibly small and completely disappeared when applying negative field strengths. The field dependency of the PES as described previously, e.g. the energy gap, is still present and thus, can be confirmed by the optimized curves, see Figure 4.9.

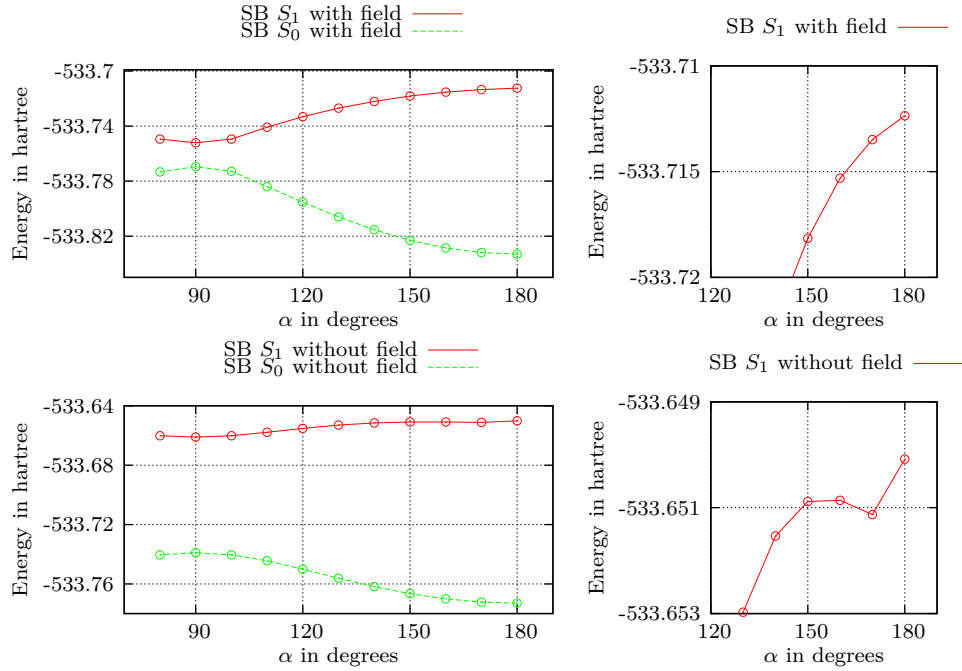


Figure 4.9.: Section planes of the DB topology. (Top left) with negative applied electric field $\mathbf{E} = -50 \frac{\text{MV}}{\text{cm}}$, (bottom left) without electric field. (Top right) zoom of the reaction barrier with applied field and without (bottom right).

The SB topology shows that negative field strengths favor the single bond twist. In detail, the very small energy barrier entirely vanishes and the energy gap between S_0 and S_1 becomes smaller, but is still present, at the examined field strengths.

4.4. Influence of the Field & Active Space

The energy gap between S_1 and S_0 of both, the single and double bond twisted structures, decreases linearly with the favoring field strength (see Figure 4.10). The absolute slope of the SB twisted structure is stronger than the slope of the DB twisted structure. Moreover, I suggest that even within SB_{\min} a conical intersection can be forced which would require, according to extrapolation, a field strength of approximately $-70 \frac{\text{MV}}{\text{cm}}$.

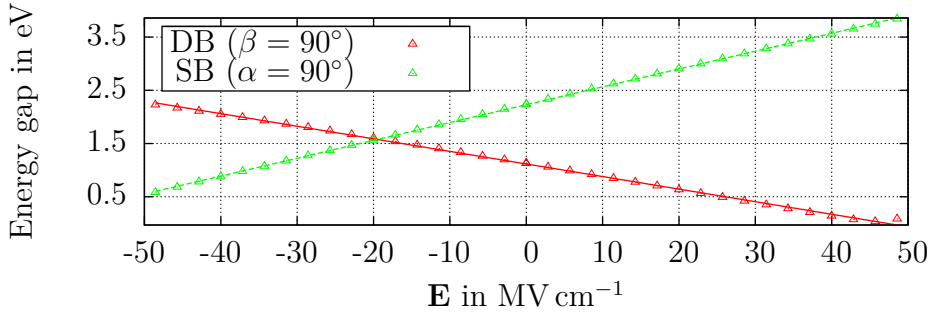


Figure 4.10.: Energy gap between S_0 and S_1 plotted against the electric field strength of the single and double bond twisted structure. The fitted parameters of the linear regression are: DB_{\min} slope= $(-0.024 \pm 0.001) \frac{\text{eV cm}}{\text{MV}}$, intercept= $(1.116 \pm 0.005) \text{ eV}$; SB_{\min} slope= $(0.033 \pm 0.001) \frac{\text{eV cm}}{\text{MV}}$, intercept= $(2.230 \pm 0.002) \text{ eV}$

Additionally, the topologies for the single and double bond twist were calculated, with a reduced active space, including six electrons and six orbitals. The topologies are presented in the appendix, see Fig. A.1 on page 43 and Fig. A.2 on page 44. In comparison to the larger active space, both SB topologies show the same curvature, except for their total energy values caused by the varied active space. However, the DB topology (Fig. A.2) demonstrates an evident difference to its larger active space analogue at first sight. The conical intersection is already present for a field strength of $25 \frac{\text{MV}}{\text{cm}}$, followed by an increasing energy gap that cannot be reasonable as the angle did not twist and therefore both dipole moments still point in the same direction. Due to the smaller active space, the electric field is strong enough to induce a transition from the first excited state to the ground state, given by the swap of the CI coefficients. The transition is graphically supported by the gradients in field direction of S_0 and S_1 for $\beta = 90^\circ$ where the slope of S_0 before the conical intersection equals the slope of S_1 afterwards, and vice versa.

5

Dynamics

After performing the single point energy calculations, this chapter is about the time-resolved simulations, including new aspects as well as confirmation of earlier results. First, the computational details and the simulation setup are discussed, followed by the question if the predicted single/double bond twist and the radiationless decay of the latter can be observed in simulations. Finally, the field dependency of the absorption spectra and a proposition for a spontaneous emission rate is presented.

5.1. Simulation Setup and Computational Details

5.1.1. Simulation Setup

The simulation setup can be split into two parts: Firstly, the chromophore which was placed at the center of the simulation box and secondly, two charged plates which are embedding the chromophore. The plates are modulated with variable charged ions to imitate a parallel plate type capacitor.

5. Dynamics

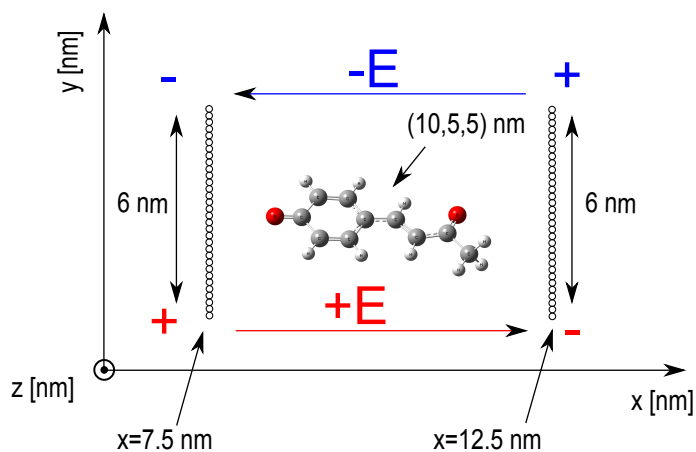


Figure 5.1.: Schematic illustration of the simulation setup

versa. Additionally, the field lines¹ are illustrated in Figure 5.2b, representing the electric field distribution between both plates.

To get a better idea of the setup, especially of the dimensions see Figure 5.1 and 5.2a. To understand the relative field orientations which will only be referred to as positive or negative in the following sections, see also Figure 5.1. If the plate next to the phenolate ring is positively charged and the other one negative, the field will be positively defined and vice

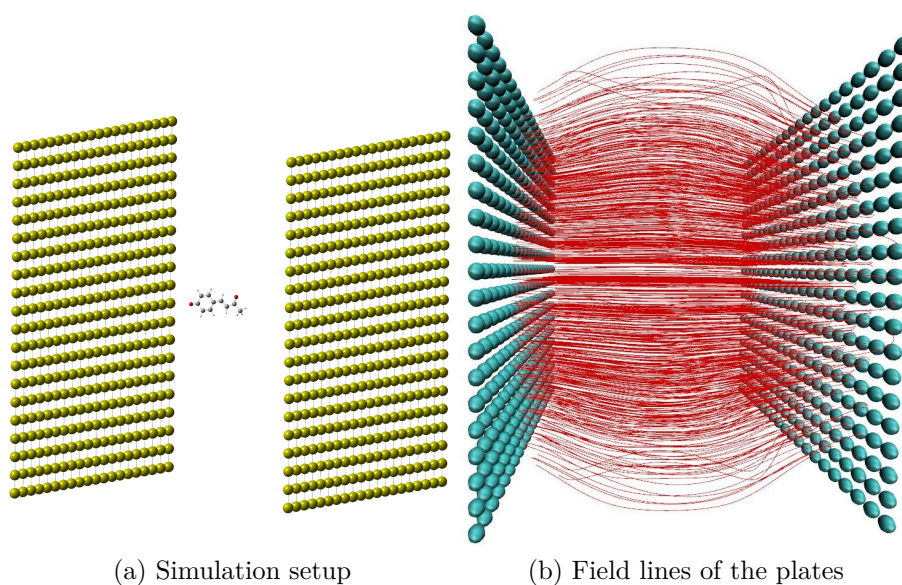


Figure 5.2.: (a) shows the simulation setup. The chromophore is placed in the center of the imitated plate type capacitor; (b) visualizes the field lines of both plates. Note that in the center of both plates the electric field lines are parallel.

The field lines are parallel to the line between the center of both plates thus, the field is homogeneous as expected from a parallel plate type capacitor. At the edges they are curving because of the limited plate size. Nevertheless, at the center, where

¹The field lines are calculated via the Poisson-Boltzmann equation plug-in of VMD [16]

the chromophore is located, the field strength can be calculated as for an infinite plate type capacitor. Overall, each plate contains 400 ions with a total area of $A = (6 \times 6) \text{ nm}^2$. The total electric field strength can be expressed as

$$\mathbf{E} = \frac{400 \cdot \tilde{q} \cdot e}{\epsilon_0 \cdot A} \quad (5.1)$$

where \tilde{q} is the variable charge of an ion, e the elementary charge and ϵ_0 the dielectric constant. For $\tilde{q} = 0.01$ the field strength becomes $\mathbf{E} = 20.3 \frac{\text{MV}}{\text{cm}}$.

5.1.2. Computational Details

To perform time-resolved simulations the QM/MM software GROMACS [1] was used. The chromophore was treated with quantum mechanics similar to the static calculations, see Section 4.1. The active space included six orbitals with six electrons, otherwise a meaningful simulation time would not have been affordable. On the contrary to the previous active space, instead of taking the canonical HF orbitals, the natural bond orbitals (NBO) were used as basis for the active space which was successively reduced where again only π/π^* orbitals were taken into account. The minor selection criterion was obtained by the one electron density matrix. More precisely, orbitals with an eigenvalue of almost 2.0 or 0.0 were ruled out.

Table 5.1.: MO selection steps for reducing the active space

active space	replaced MOs
(10e,11o)	(39,38) \leftrightarrow (37,36)
(10e,10o)	-
(10e,9o)	-
(8e,8o)	-
(8e,7o)	47 \leftrightarrow 45
(6e,6o)	41 \leftrightarrow 40

¹ Instead of 12 electrons the starting active space contains only 10 as the orbitals are not in correct order.

For the detailed orbital selection, see Table 5.1.

Most of the simulations were performed via the GAUSSIAN plug-in for GROMACS. The MOLPRO plug-in was only used for calculating the transition dipole moments (see Section 5.5) and to double check selected results. Again the 6-31G* basis set and the state averaging method for the ground and first excited state were applied with both weights taken equally as 0.5. The time step was set to 0.5 fs and the convergence energy and gradient threshold for GAUSSIAN was appointed to 10^{-6} a.u. which is consistent with a moderate accuracy but is a necessity for the required simulation times (1-2 ps).

For the molecular mechanics part, including the angle and dihedral dependency of the chromophore, the amber 99 force field [5] was

5. Dynamics

applied. Furthermore, all starting momenta were randomly generated but obey the Maxwell distribution for 300 K. All simulations have been performed using periodic boundaries with a box size of $20 \times 10 \times 10$ nm as well as a coulomb cutoff with a radius of 5 nm. To ensure that the ions do not interact with each other exclusions were applied. Moreover, to keep the chromophore always at the center of the box, a position constraint for the oxygen atom, located at the ring structure, was placed, otherwise the chromophore would move due to its net charge.

5.1.3. Ground State Ensemble

The first step before simulating excited state dynamics was the establishment of a ground state ensemble. After a classical MD simulation over 30 ns (0.1 ps step size), six trajectories with a total length of 2000 steps each were received using QM/MM. The applied electric field had a strength of $20 \frac{\text{MV}}{\text{cm}}$, so the molecule could adjust to the field lines. Thus, the same situation as in the static calculations, where the electric field was applied parallel to μ_0 of the planar minimum, was obtained. The positive strength was arbitrarily chosen with the only constraint that it is strong enough to adjust the chromophore. I might have chosen negative strengths as well, but the necessary simulation time for adjusting the chromophore to the field lines would be much higher as it has to rotate around 180° (see the starting position in Figure 5.1 on page 30). Finally, for getting the ensemble new starting structures were extracted from the equilibrium trajectories. More precisely, the first structure was obtained after the 800th step followed by three more every 400 steps, so that overall the ensemble contained 24 structures.

5.2. Control of the Single/Double Bond Twist

The focus of this section lies on the question whether or not the excited state dynamics of pCK^- can be controlled by electric fields. Therefore, three different field strength $\mathbf{E} \in \{-20 \frac{\text{MV}}{\text{cm}}; 0.0 \frac{\text{MV}}{\text{cm}}; 20 \frac{\text{MV}}{\text{cm}}\}$ were chosen according to the results of the static simulations in Chapter 4, although they did not match the maximal/minimal used field strengths.

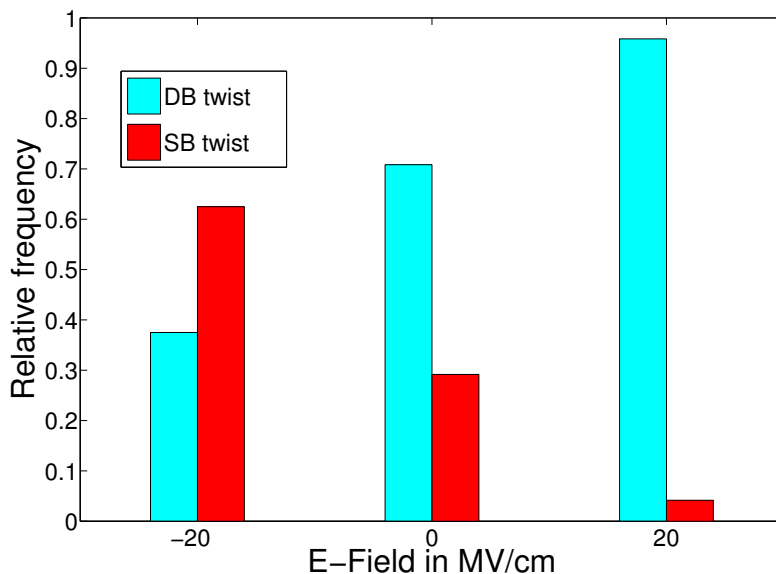


Figure 5.3.: Relative frequencies of single and double bond twisted structures for different field strengths. For each strength 24 simulations were performed.

For every field strength the generated ensemble had been simulated in the excited state as long as all trajectories were either in SB_{min} or DB_{min} . The results are illustrated in Figure 5.3 where the relative frequencies are shown for different field strengths. The effect which is supported by the static investigations can be approved by the simulations. If the field strength is positive i.e. see Figure 5.1, almost all trajectories will go into the DB twist. On the contrary, the SB twist is favored by a negative field, although the distribution is not as clear as for the DB. According to the field influence of SB_{min} , see 4.10 on page 27, the distribution will even more favor the SB twist while increasing the negative field strength. Even though the results confirm the previously calculated PES, the predicted predominance of the SB structure - according to the topologies (see Figure 4.6 on page 24 and Figure 4.2 on page 20) - could not be found. The topologies were performed with respect to

5. Dynamics

one degree of freedom, so they serve as a oversimplified model but do not reflect reality. On the contrary, the time-resolved simulations depend on on all internal coordinates. As an example of the discussed trajectories, Figure 5.4 shows the time evolution of the energy gap between both states and its corresponding torsion angle, whereas the field strength was set to zero. Both excited state twisting processes behave related, when the single/double bond angle equals 90° the energy gap becomes minimal which implies that the SB_{\min}/DB_{\min} is reached. Moreover, in this example the SB twist occurs faster than the DB twist which is in good agreement with the described curvature of the PESs and its missing barrier, see Section 4.3.

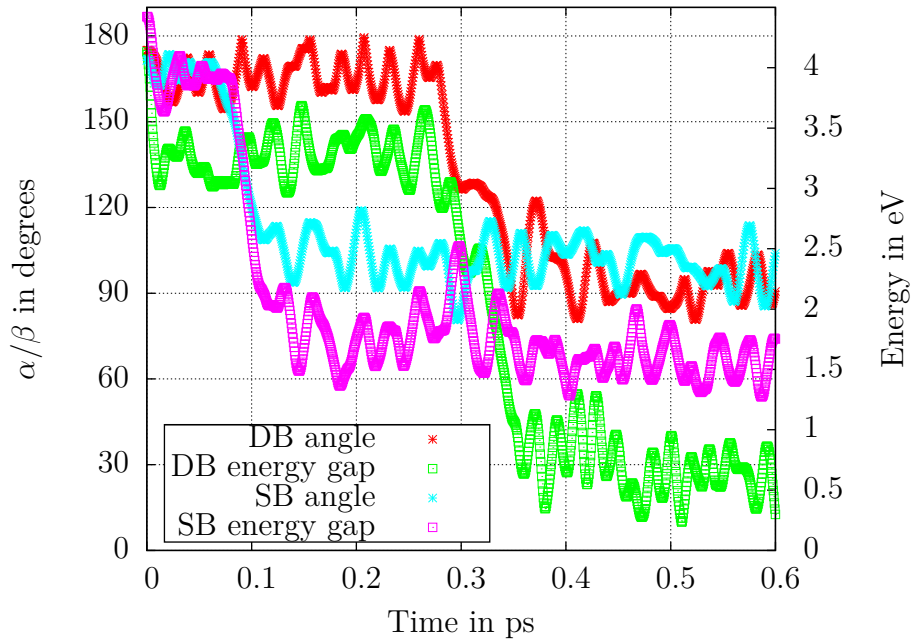


Figure 5.4.: Example of the single and double bond twist. The time evolution of the energy gaps $|S_1 - S_0|$ and torsion angles without electric field is shown.

5.3. Radiationless Decay

The next step is to focus on the DB twist and its expected radiationless decay. The goal is to determine the rate of the radiationless decay, assuming a simple exponential decay. The field strength $\mathbf{E} = 20 \frac{\text{MV}}{\text{cm}}$ was chosen for the simulation of the ensemble. According to Figure A.2 on page 44, the used field strength favors the conical intersection; for a smaller field the simulation time would increase exponentially. Unfortunately, within the time interval of 3.5 ps only 14 of 23 radiationless decays² could be observed. To determine the rate the number of observed decay events $N(t)$ is assumed to be proportional to $e^{k \cdot t}$ where k represents the decay rate. Figure 5.5 shows a half-logarithmic plot for $N(t)$ where k is determined as the slope which is $k = (0.80 \pm 0.13) \text{ ps}^{-1}$.

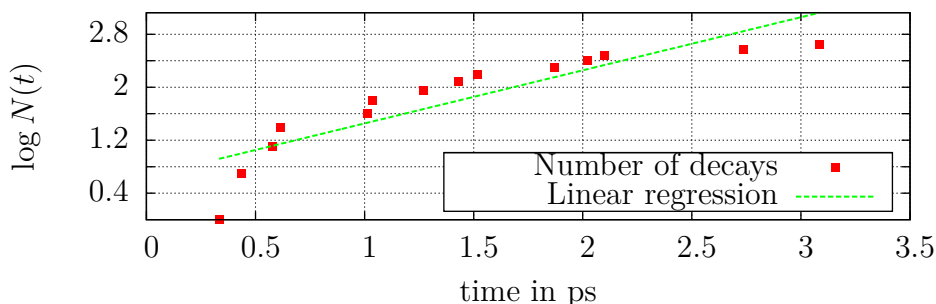


Figure 5.5.: Half-logarithmic plot of the observed number of radiationless decays to determine the decay rate k . The obtained parameters are: slope= $(0.80 \pm 0.13) \text{ ps}^{-1}$ and intercept= 0.65 ± 0.21 .

The obtained rate is in close agreement with experimentally observed fluorescence decay rates in solution. Espagne et al. [7] measured the fluorescence decay rate for pCK⁻ in aqueous solution using steady-state spectroscopy to be 0.77 ps^{-1} . Even though they did not directly apply electric fields, the strong dipole moments of the water molecules induce local electric fields. I suggest that these induced fields are in the order of the applied external electric fields and therefore accelerate the decay. In any case, according to [3], hydrogen bonds are stabilizing the single and double bond twisted minimum, with respect to S_0 . Moreover, they lower the energy gap between S_0 and S_1 in the DB minimum, while the gap of the SB minimum is increased. Figure 5.6 shows the influence of hydrogen bonds for the

²The 24th was falling into the SB_{min}.

5. Dynamics

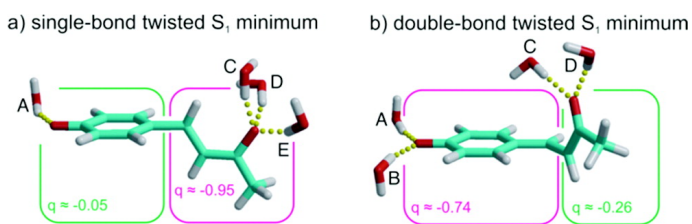


Figure 5.6.: Hydrogen Bonds linked to the SB/DB twisted structure. Additionally, the mulliken charge distributions are shown. [3]

single/double bond twist. According to simulations of Boggio-Pacqua et al. [3], within the SB twist three water molecules are involved nearby the carbonyl tail, whereas one weak hydrogen bond is located at the phenolate group. In the case of the

DB twist, at least two strong hydrogen bonds were found to influence the phenolate group but only one or two weak bonds were found influencing the carbonyl tail. According to the mulliken charge distribution, the hydrogen bonding patterns do not only reflect the charge distribution (see Figure 3.3 on page 14) but rather increase the charge transfer of the respective excited state minimum.

As an example for the surface hopping Figure 5.7 shows the time-resolved DB twist and the following intersection. At 0.2 ps the system evolves from the planar minimum into DB_{\min} and at 0.6 ps the energy gap becomes zero, the chromophore falls back to the ground state and finally moves back to the planar minimum (trans-isomer).

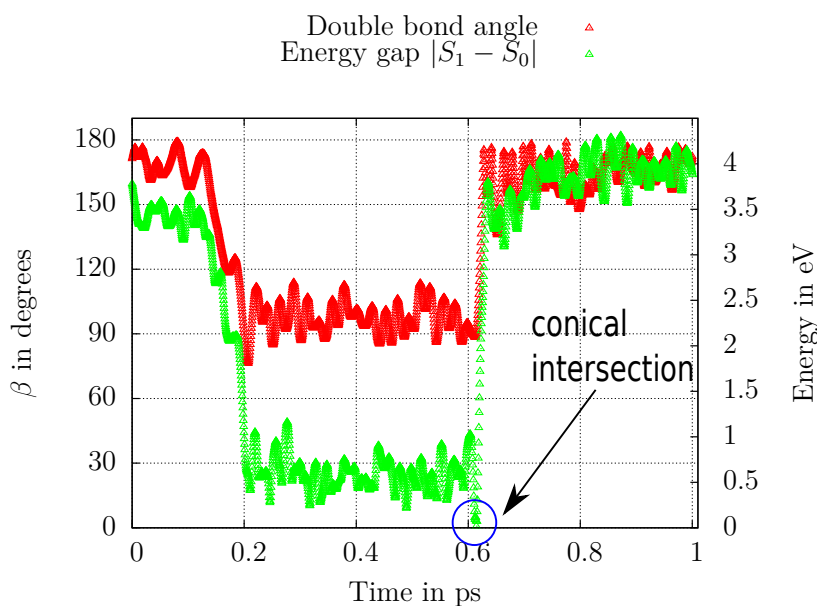


Figure 5.7.: Example for a radiationless decay transition. The time evolution of the DB torsion angle and its corresponding energy gap is shown.

As previously pointed out, in addition to the trans-isomerization also the cis-isomerization exists. Here β changes from 90° to 0° (see Figure 5.8), so that all carbon atoms are aligned in the same plane. The number of cis/trans transitions was counted for the observed radiationless decays (see Figure 5.5). 10 of the 14 trajectories were falling into the trans minimum but, at least, four trajectories showed the cis-isomer. The quantum yield of the cis-isomer is approximately 29%, which is in good agreement with the observed quantum yield for the cis-isomerization of pCA in PYP experimentally [15] as well as in former calculations [10].

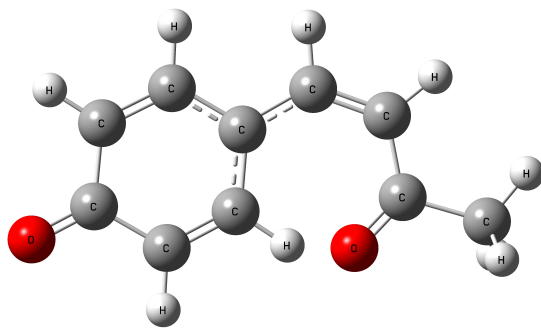


Figure 5.8.: Cis-isomer of the pCK⁻ chromophore

5.4. Absorption Spectra

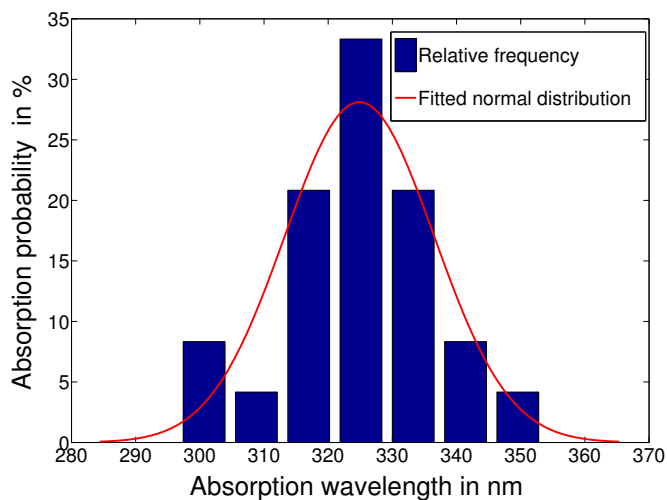


Figure 5.9.: Single absorption spectrum for $\mathbf{E} = -20 \frac{\text{MV}}{\text{cm}}$

In this section the absorption spectra of pCK^- are investigated. The focus lies on the question if and how the absorption spectra are influenced by electric fields. The initial point was again the ground state ensemble in the planar minimum where each structure got excited and the energy gap between S_0 and S_1 was calculated. Subsequently, this procedure was repeated for five different field strengths and on the basis of the data normalized histograms were created and normal distributions were fitted against them. Note that each absorption spectrum is based on the same ground state ensemble. An arbitrary example for such a histogram as well as its Gaussian fit is shown in Figure 5.9. Even though the ensemble is comparatively small, a normal distribution can be recognized.

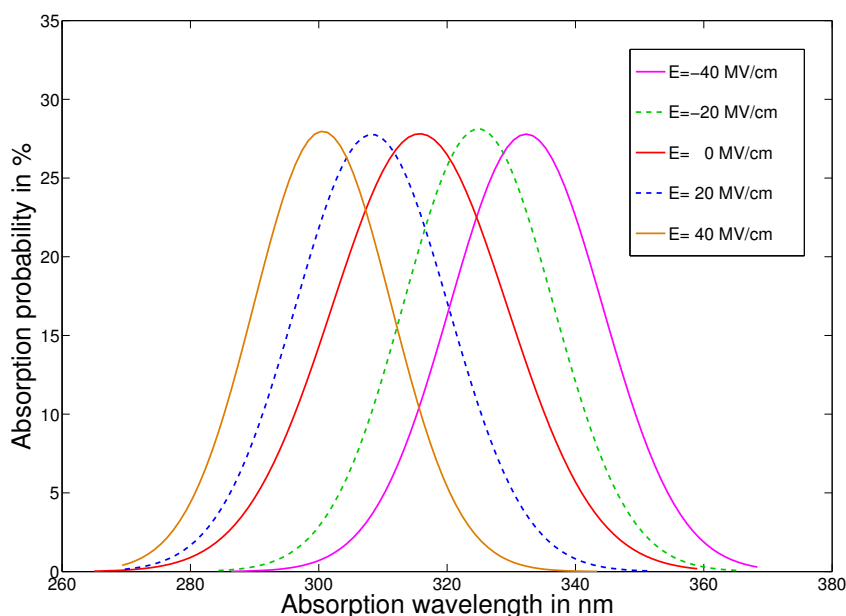


Figure 5.10.: Gaussian fitted absorption curves for five different field strengths

The influence of the electric field is illustrated in Figure 5.10 where an obvious shift of the field spectra is observable. For negative field strengths the absorption wavelength are larger than for positive ones which is in good agreement with the static calculations (see Section 4.3 and 4.2) where the energy gap increases with positive field strengths. Furthermore, the shift seems to be proportional to the field strength and also the shapes of the Gaussians, which are determined by the standard deviations, are very similar. However, this is reasonable as, according to the linear Stark Effect, the electric field couples with the dipole moment $\boldsymbol{\mu}_i$ of the respective state. The electric field is treated as perturbation, leading to the first order energy correction

$$E^{(1)} = \langle \psi_i^0 | H_1 | \psi_i^0 \rangle = -\mathbf{E} \cdot \langle \psi_i^0 | \boldsymbol{\mu} | \psi_i^0 \rangle = -\mathbf{E} \cdot \langle \boldsymbol{\mu}_i \rangle. \quad (5.2)$$

Hence, whether or not the system gains energy depends only on the direction of the electric field relative to $\boldsymbol{\mu}_i$. The positive field strengths in Figure 5.10 matches the direction of $\boldsymbol{\mu}_0$ but not of $\boldsymbol{\mu}_1$ (see Section 3.2), and therefore the energy difference between S_0 and S_1 , only caused by the electric field is described by:

$$\Delta E = \pm |\mathbf{E}| \cdot (|\langle \boldsymbol{\mu}_0 \rangle| - |\langle \boldsymbol{\mu}_1 \rangle \cos \vartheta|) \quad (5.3)$$

where ϑ is the angle between the electric field and $\boldsymbol{\mu}_1$. The energy shift is linear with the applied field strength as the second term is constant, because only the planar minimum structure was excited.

5.5. Spontaneous Emission

The last section is based on several assumptions. If the chromophore evolves into the SB minimum, the energy gap will be too large for a radiationless decay. Assuming that the barriers next to the minimum are high enough, the chromophore is forced to stay at SB_{\min} until a radiative decay can occur. This section provides the rate for a spontaneous emission from the first excited state to the ground state at SB_{\min} and its dependency on the electric fields.

The rate Γ for spontaneous emission is proportional to the Einstein coefficient (for

5. Dynamics

a derivation see [19]) and can be expressed as

$$\Gamma_{1 \rightarrow 0} = \frac{64\pi^4 \nu_{10}^3}{3hc^2} \cdot |\langle 1 | \hat{\mathbf{d}} | 0 \rangle|^2 \quad (5.4)$$

where ν_{10} is the frequency of the photon, being proportional to the energy gap between S_1 , and S_0 and $\hat{\mathbf{d}}$ the transition dipole operator. To obtain ν_{10} and $\langle 1 | \hat{\mathbf{d}} | 0 \rangle$ the SB minimum was simulated about 0.5 ps, while applying different field strengths. Overall, the field was varied from $-40 \frac{\text{MV}}{\text{cm}} \leq \mathbf{E} \leq 0 \frac{\text{MV}}{\text{cm}}$ with a step size of $\Delta \mathbf{E} = 4 \frac{\text{MV}}{\text{cm}}$ where three trajectories for each strength had been performed. In contrast to the previous section, all trajectories started with the same structure, otherwise structural change would lead to strong differences within the same field strengths. To achieve the rate for one field strength, the mean value of both, the transition dipole moments and energy gaps including all 500 steps, belonging to one trajectory, had been taken. Then the mean value of all three trajectories was evaluated. Figure 5.11 shows the rate dependency of the field strength which is apparently linear at least for the investigated interval. Furthermore, a linear regression had been performed with exclusion of the strongly deviated value $\mathbf{E} = -33 \frac{\text{MV}}{\text{cm}}$. The obtained linear function is:

$$\Gamma(\mathbf{E}) = 1.1 \frac{\text{cm}}{\text{ns MV}} \cdot \mathbf{E} + 72.5 \text{ ns}^{-1} \quad (5.5)$$

and thus, can be evaluated as direct proportional to the applied field strength. The intercept depends on the starting structure and therefore has less significance. According to Eq. 5.4 and the linear dependency of Eq. 5.5, the transition dipole moment $|\langle 1 | \hat{\mathbf{d}} | 0 \rangle|$ is proportional to $|\frac{1}{E_1 - E_0}|$.

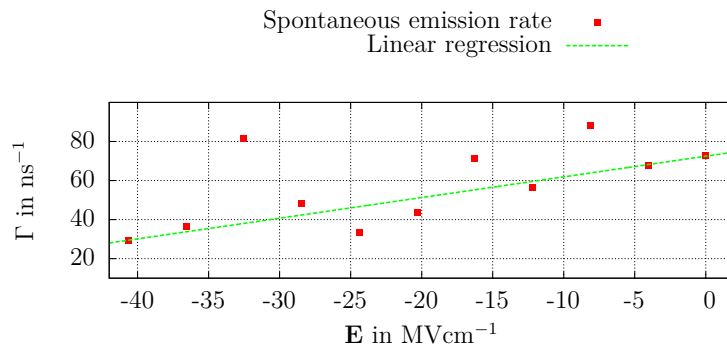


Figure 5.11.: Field dependency of the rate for spontaneous emission from S_1 to S_0 at the single bond minimum. The fitted parameters are: slope $m = (1.1 \pm 0.2) \frac{\text{cm}}{\text{ns MV}}$; intercept $b = (72.5 \pm 5.5) \text{ ns}^{-1}$.

6

Conclusion & Outlook

In this thesis, the topology of the ground and first excited state for both possible torsion angles (α and β) of the pCK⁻ chromophore were presented. The electric fields show a significant effect on the topologies of the single and double bond twisted structure. In detail, not only the applied field strength but also the orientation of the field determines whether the single bond or double bond twist is favored. The single bond twist is supported by negative field strengths and the double bond twist is supported by positive field strengths where the orientation is given relative to the ground state dipole moment of the planar structure. Moreover, by increasing the positive field strength the surfaces can be forced to intersect. In the second part, the achieved topologies were validated through dynamic simulations. The predicted influence of the field could be observed. Even if the field strengths of the time-resolved simulations are ten times larger than experimentally feasible ones - at least by using a capacitor - I think that the field influence can still be experimentally validated because the relative frequency of the single/double bond twisted structure increases linearly with its corresponding field strength (see Figure 5.3 on page 33). Additionally, the rate of the radiationless decay was obtained; it is similar to experimentally measured rates in aqueous solution, but without external electric fields. I suggest that the water molecules induce local electric fields being of the same magnitude

6. Conclusion & Outlook

as the applied external ones. Furthermore, the field dependency of the absorption spectra was examined as well as an attempt was made to predict the radiative decay rate.

The next consequent step would be the experimental validation of the theoretically obtained results. Nakabayashi et al.[21] examined the field-induced changes in absorption and fluorescence of the GFP chromophore and Espagne et al. [6] also did absorption and fluorescence experiments with pCK⁻, although without electric fields.

Besides the experimental validation, further numerical calculations could include the effect of solvents additionally to the field influence which could favor the double bond twist even more. Another interesting question would be, if the single bond twist could be completely inhibited by an additional ethylene group connected to the phenolate ring.

However, the steering of excited state dynamics by electric fields makes several applications imaginable, for instance, a pixel could be established where the electric field acts as a switch for either color (SB twist) or no color (DB twist). Another possible application could be a molecular engine as the double bond isomerization is fully reversible, thus light energy would be converted into kinetic energy. Nevertheless, I hope that the results of this work will trigger further investigations of the influence of electric fields in photoisomerization and maybe it will form the basis of future technology.

A

Appendix

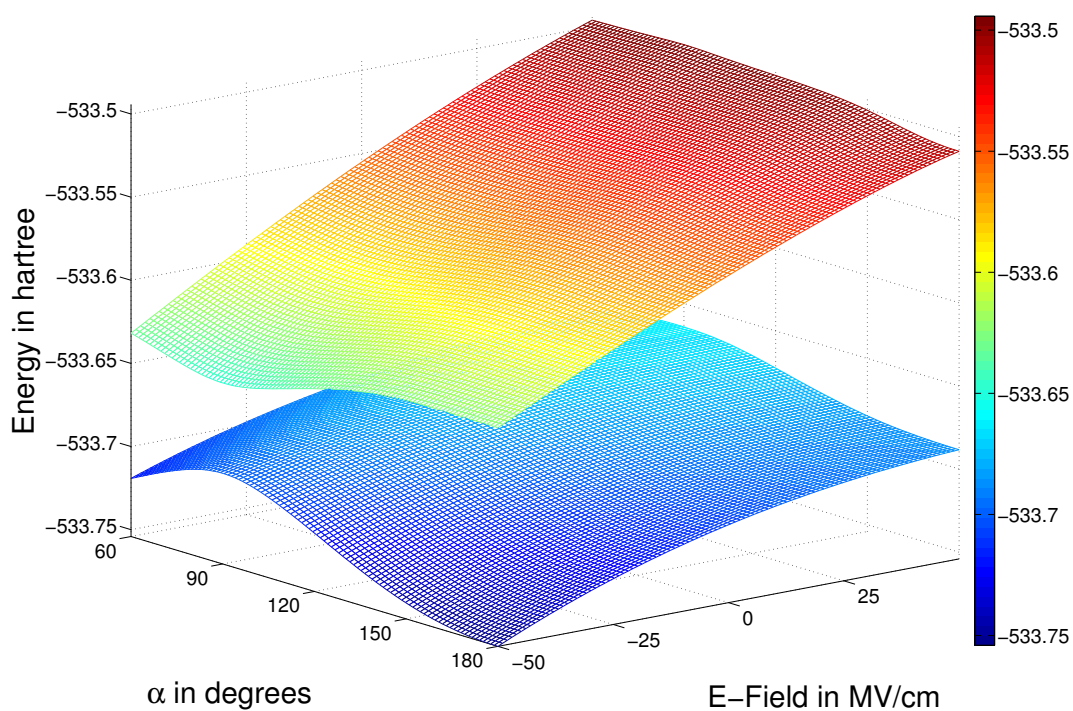


Figure A.1.: PESs of S_0 and S_1 after performing CASSCF(6e,6o) without geometry optimization. The total energy of S_0 and S_1 is plotted against the electric field strength \mathbf{E} and the SB torsion angle α .

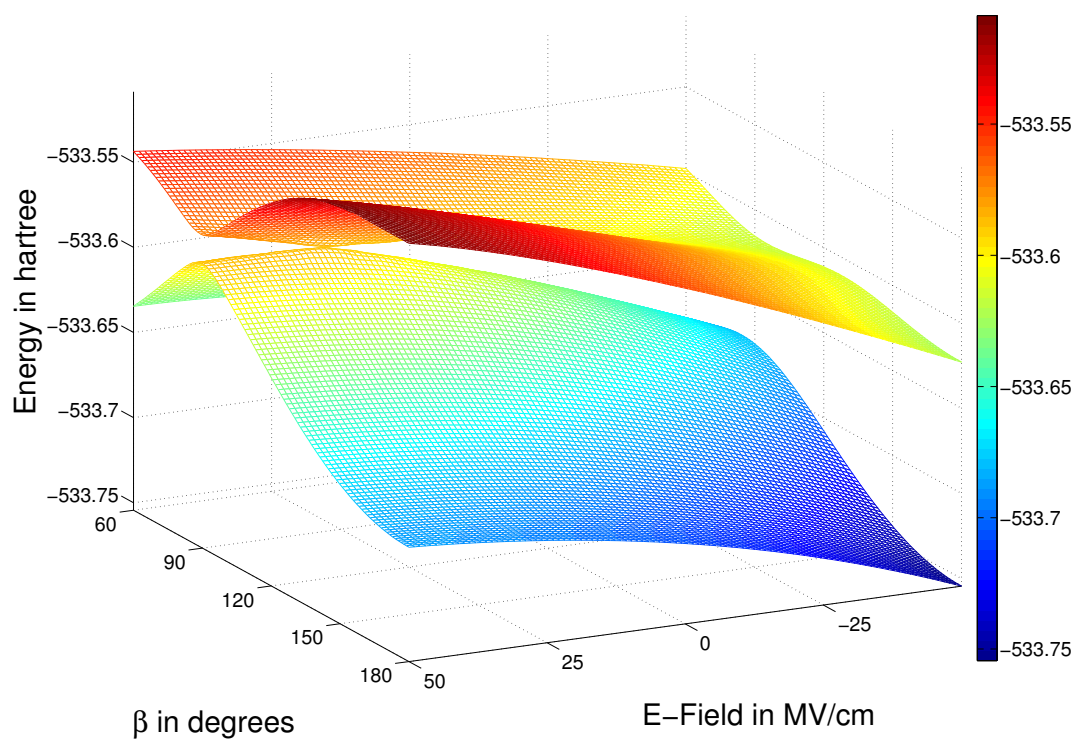


Figure A.2.: PESs of S_0 and S_1 after performing CASSCF(6e,6o) without geometry optimization. The total energy of S_0 and S_1 is plotted against the electric field strength \mathbf{E} and the DB torsion angle β .

Bibliography

- [1] Emile Apol, Rossen Apostolov, Herman J.C. Berendsen and Aldert van Buuren, Pär Bjelkmar, Rudi van Drunen, Anton Feenstra, Gerrit Groenhof, Peter Kasson, Per Larsson, Pieter Meulenhoff, Teemu Murtola, Szilard Pall, Sander Pronk, Roland Schulz, Michael Shirts, Alfons Sijbers, Peter Tieleman, Berk Hess, David van der Spoel, , and Erik Lindahl. Gromacs version 4.5.3, 2010.
- [2] R.R. Birge. Nature of the primary photochemical events in rhodopsin and bacteriorhodopsin. *Biochim. Biophys. Acta*, 1016(3):293–327, 1990.
- [3] M. Boggio-Pasqua, M.A. Robb, and G. Groenhof. Hydrogen bonding controls excited-state decay of the photoactive yellow protein chromophore. *Journal of the American Chemical Society*, 131(38):13580–13581, 2009.
- [4] Carl Burmeister. Interaction of short x-ray pulses with small molecules. Master’s thesis, Department for Theoretical and Computational Biophysics Max Planck Institute for Biophysical Chemistry, Göttingen, 2009.
- [5] D.A. Case, T.A. Darden, T.E. Cheatham, C.L. Simmerling, J. Wang, R.E. Duke, R. Luo, R.C. Walker, W. Zhang, K.M. Merz, B. Roberts, B. Wang, S. Hayik, A. Roitberg, G. Seabra, I. Kolossvai, K.F. Wong, F. Paesani, J. Vanicek, J. Liu, X. Wu, S.R. Brozell, T. Steinbrecher, H. Gohlke, Q. Cai, X. Ye, J. Wang, M.-J. Hsieh, G. Cui, D.R. Roe, D.H. Mathews, M.G. Seetin, C. Sagui, V. Babin, T. Luchko, S. Gusarov, A. Kovalenko, and P.A. Kollman. Amber 11, 2010.
- [6] A. Espagne, D.H. Paik, P. Changenet-Barret, M.M. Martin, and A.H. Zewail. Ultrafast photoisomerization of photoactive yellow protein chromophore analogues in solution: Influence of the protonation state. *ChemPhysChem*, 7(8): 1717–1726, 2006.

Bibliography

- [7] A. Espagne, D.H. Paik, P. Changenet-Barret, P. Plaza, M.M. Martin, and A.H. Zewail. Ultrafast light-induced response of photoactive yellow protein chromophore analogues. *Photochem. Photobiol. Sci.*, 6(7):780–787, 2007.
- [8] M. J. Frisch, G. W. Trucks, H. B. Schlegel, G. E. Scuseria, M. A. Robb, J. R. Cheeseman, G. Scalmani, V. Barone, B. Mennucci, G. A. Petersson, H. Nakatsuji, M. Caricato, X. Li, H. P. Hratchian, A. F. Izmaylov, J. Bloino, G. Zheng, J. L. Sonnenberg, M. Hada, M. Ehara, K. Toyota, R. Fukuda, J. Hasegawa, M. Ishida, T. Nakajima, Y. Honda, O. Kitao, H. Nakai, T. Vreven, J. A. Montgomery, Jr., J. E. Peralta, F. Ogliaro, M. Bearpark, J. J. Heyd, E. Brothers, K. N. Kudin, V. N. Staroverov, R. Kobayashi, J. Normand, K. Raghavachari, A. Rendell, J. C. Burant, S. S. Iyengar, J. Tomasi, M. Cossi, N. Rega, J. M. Millam, M. Klene, J. E. Knox, J. B. Cross, V. Bakken, C. Adamo, J. Jaramillo, R. Gomperts, R. E. Stratmann, O. Yazyev, A. J. Austin, R. Cammi, C. Pomelli, J. W. Ochterski, R. L. Martin, K. Morokuma, V. G. Zakrzewski, G. A. Voth, P. Salvador, J. J. Dannenberg, S. Dapprich, A. D. Daniels, Ö. Farkas, J. B. Foresman, J. V. Ortiz, J. Cioslowski, and D. J. Fox. Gaussian 09 Revision A.1, 2009. Gaussian Inc. Wallingford CT 2009.
- [9] Boggio-Pasqua Martial; Groenhof Gerrit. Controlling the photoreactivity of the photoactive yellow protein chromophore by substituting at the p-coumaric acid group. *JOURNAL OF PHYSICAL CHEMISTRY B*, 115(21):7021–7028, 2011.
- [10] G. Groenhof, M. Bouxin-Cademartory, B. Hess, S.P. de Visser, H.J.C. Berendsen, M. Olivucci, A.E. Mark, and M.A. Robb. Photoactivation of the photoactive yellow protein: Why photon absorption triggers a trans-to-cis isomerization of the chromophore in the protein. *Journal of the American Chemical Society*, 126(13):4228–4233, 2004.
- [11] Gerrit Groenhof. *Understanding Light-Induced Conformational Changes in Molecular Systems from First Principles*. PhD thesis, University of Groningen, 2005.
- [12] Gerrit Groenhof, Martial Boggio-Pasqua, Lars V. Schäfer, and Michael A. Robb. *Advances in Quantum Chemistry Vol. 59 /Chapter 6 - Computer Simulations of Photobiological Processes: The Effect of the Protein Environment*. Elsevier Inc, 2011.

- [13] Evgeniy V Gromov, Irene Burghardt, James T Hynes, H Koppel, and Lorenz S Cederbaum. Electronic structure of the photoactive yellow protein chromophore: Ab initio study of the low-lying excited singlet states. *Journal of Photochemistry and Photobiology A: Chemistry*, 190(2-3):241–257, 2007.
- [14] P. J. Knowles H.-J. Werner. *User Manual Version 2006.1*, 2006.
- [15] K.J. Hellingwerf, J. Hendriks, and T. Gensch. Photoactive yellow protein, a new type of photoreceptor protein: Will this "yellow lab" bring us where we want to go? *The Journal of Physical Chemistry A*, 107(8):1082–1094, 2003.
- [16] William Humphrey, Andrew Dalke, and Klaus Schulten. VMD – Visual Molecular Dynamics. *Journal of Molecular Graphics*, 14:33–38, 1996.
- [17] Frank Jensen. *Introduction to Computational Chemistry*. Wiley, 2007.
- [18] C. Ko, B. Levine, A. Toniolo, L. Manohar, S. Olsen, H.J. Werner, and T.J. Martínez. Ab initio excited-state dynamics of the photoactive yellow protein chromophore. *Journal of the American Chemical Society*, 125(42):12710–12711, 2003.
- [19] Ira N. Levine. *Molecular Spectroscopy*. John Wiley and Sons, 1975.
- [20] Ira N. Levine. *Quantum Chemistry*. Pearson International Edition, 2008.
- [21] Takakazu Nakabayashi, Kazuyuki Hino, Yuka Ohta, Sayuri Ito, Hirofumi Nakano, and Nobuhiro Ohta. Electric-field-induced changes in absorption and fluorescence of the green fluorescent protein chromophore in a pmma film. *The Journal of Physical Chemistry B*, 115(26):8622–8626, 2011.
- [22] Wolfgang Nolting. *Grundkurs Theoretische Physik 5/2: Quantenmechanik - Methoden und Anwendungen*. Springer, 2006.
- [23] R.R. Rando. The biochemistry of the visual cycle. *Chemical Reviews*, 101(7):1881–1896, 2001.
- [24] W.W. Sprenger, W.D. Hoff, J.P. Armitage, and KJ Hellingwerf. The eubacterium *ectothiorhodospira halophila* is negatively phototactic, with a wavelength dependence that fits the absorption spectrum of the photoactive yellow protein. *Journal of bacteriology*, 175(10):3096, 1993.

Bibliography

- [25] Oliver Weingart. *Ab initio Moleküldynamik der Photoisomerisierung von protonierten Polyenaldehyd Schiff Basen*. PhD thesis, Universität Duisburg-Essen, 2005.
- [26] H.-J. Werner, P. J. Knowles, G. Knizia, F. R. Manby, M. Schütz, P. Celani, T. Korona, R. Lindh, A. Mitrushenkov, G. Rauhut, K. R. Shamasundar, T. B. Adler, R. D. Amos, A. Bernhardsson, A. Berning, D. L. Cooper, M. J. O. Deegan, A. J. Dobbyn, F. Eckert, E. Goll, C. Hampel, A. Hesselmann, G. Hetzer, T. Hrenar, G. Jansen, C. Köppl, Y. Liu, A. W. Lloyd, R. A. Mata, A. J. May, S. J. McNicholas, W. Meyer, M. E. Mura, A. Nicklass, D. P. O'Neill, P. Palmieri, K. Pflüger, R. Pitzer, M. Reiher, T. Shiozaki, H. Stoll, A. J. Stone, R. Tarroni, T. Thorsteinsson, M. Wang, and A. Wolf. Molpro, version 2010.1, a package of ab initio programs, 2010. see <http://www.molpro.net>.

Acknowledgement

Ich möchte zuallerst meinem Betreuer Dr.Gerrit Groenhof danken, ohne dessen Idee diese Arbeit gar nicht erst entstanden wäre. Besonders durch seine *open-door policy*, so stand er mir fast täglich bei kleinen und größeren Problemen mit Rat und Tat zur Seite, trug er erheblich zum Erfolg dieser Arbeit bei.

Weiterhin möchte ich meinen Bürokollegen Carl Burmeister und Ludger Inhester, sowie Timo Graen danken. Jeder dieser drei wurde nicht müde sich vor allem der alltäglichen kleinen technischen Probleme anzunehmen.

Zusätzlich möchte ich noch Prof.Dr.Helmut Grubmüller danken, dass er sich bereit erklärt hat diese Arbeit als Zweitkorrektor zu bewerten.

Als letztes danke ich meiner Freundin Imke für ihre emotionale und vor allem orthografische Unterstützung, sowie meiner Mutter für ihre finanzielle Hilfe, ohne die mein Studium und damit diese Arbeit nicht möglich wäre.

Erklärung nach §13(8) der Prüfungsordnung für den Bachelor-Studiengang Physik und den Master-Studiengang Physik an der Universität Göttingen:

Hiermit erkläre ich, dass ich diese Abschlussarbeit selbständig verfasst habe, keine anderen als die angegebenen Quellen und Hilfsmittel benutzt habe und alle Stellen, die wörtlich oder sinngemäß aus veröffentlichten Schriften entnommen wurden, als solche kenntlich gemacht habe.

Darüberhinaus erkläre ich, dass diese Abschlussarbeit nicht, auch nicht auszugsweise, im Rahmen einer nichtbestanden Prüfung an dieser oder einer anderen Hochschule eingereicht wurde.

Göttingen, den September 6, 2011

(Fabian Knoch)